A fast bow shock location predictor-estimator from 2D and 3D analytical models: Application to Mars and the MAVEN mission

Cyril Simon Wedlund[1], Martin Volwerk[1], Arnaud Beth[2], Christian Mazelle[3], Christian Möstl[1], Jasper Halekas[4], Jacob Gruesbeck[5], and Diana Rojas-Castillo[6]

[1]Space Research Institute, Austrian Academy of Sciences, Graz, Austria

[2]Department of Physics, Umeå University, 901 87 Umeå, Sweden

[3]Institut de Recherche en Astrophysique et Planétologie (IRAP), Université de Toulouse, CNRS, UPS, CNES, Toulouse, France

[4]Department of Physics and Astronomy, University of Iowa, Iowa City, IA, USA

[5]NASA Goddard Space Flight Center, Laboratory for Planetary Magnetospheres, Greenbelt, MD, USA

[6]Instituto de Geofísica, Universidad Nacional Autónoma de México, Coyoacán, Mexico

Key Points:

- More than $14,900$ bow shock crossings are identified with MAVEN for Mars Year 32 to 35, with 2D/3D fits revealing North-South asymmetries.
- The method, biased towards quasi-perpendicular crossings, is general and applicable to all planetary bodies including Mars, Venus and Earth.
- A simple predictor-corrector algorithm based on magnetic field data is presented to locate the bow shock position.

Corresponding author: C. Simon Wedlund, cyril.simon.wedlund@gmail.com

Abstract

We present general empirical analytical equations of bow shock structures historically used at Mars, and show how to estimate automatically the statistical position of the bow shock with respect to spacecraft data from 2D polar and 3D quadratic fits. Analytical expressions of bow shock normal in 2D and 3D are given for any point on the shock's surface. This empirical technique is applicable to any planetary environment with a defined shock structure. Applied to the Martian environment and the NASA/MAVEN mission, the predicted shock location from ephemerides data is on average within 0.15 planetary radius R_p of the actual bow shock crossing as seen from magnetometer data. Using a simple predictor-corrector algorithm based on the absolute median deviation of the total magnetic field and the general form of quasi-perpendicular shock structures, this estimate is further refined to within a few minutes of the true crossing ($\approx 0.05\,R_p$). With the refined algorithm, 14,929 bow shock crossings, predominantly quasi-perpendicular, are detected between 2014 and 2021. Analytical 2D conic and 3D quadratic surface fits, as well as standoff distances, are given for Martian years 32 to 35, for several (seasonal) solar longitude ranges and for two solar EUV flux levels. Although asymmetry in Y and Z Mars Solar Orbital coordinates is on average small, it is shown that for Mars years 32 and 35, Ls = [135 − 225°] and high solar flux, it can become particularly noticeable and is superimposed to the usual North-South asymmetry due to the presence of crustal magnetic fields.

Plain Language Summary

[enter your Plain Language Summary here or delete this section]

1 Introduction

Historically, planetary bow shocks, their position, size and shape, have been characterised statistically with the use of (empirical) analytical fitting models in two-dimensional (2D) or three-dimensional (3D) coordinates. A classical start point for characterising the Earth's bow shock in 3D include the seminal work of Formisano (1979), who investigated the asymmetry of the shock with respect to the apparent solar wind flow direction with the use of quadratic surface fits with 9 free parameters. In parallel, other studies such as that of Slavin and Holzer (1981) relied on a simple polar equation assuming axisymmetry along the Sun-planet line corrected by the apparent motion of the solar wind in the rest frame of the planet, the so-called aberrated X axis. The 2D approach has the merit of needing only 3 free parameters but ig-

nores the potential asymmetries of the shock as for example seen at Earth's bow shock (e.g., Formisano, 1979; Peredo et al., 1993, 1995; Merka et al., 2005).

More advanced physics-based models have also been proposed as a complement to those empirical attempts. A good introduction into analytical models of the bow shock, based on gas dynamic theory and magnetohydrodynamics solutions, is given in Verigin et al. (2003) and recently in Kotova et al. (2021). These studies present analytical functions describing the curvature, bluntness and skewing angle of the shock structure, which are arguably better suited to the fitting of the shock flanks; they are applicable to many planetary bow shock conditions.

At Mars, due to the sparsity of early data and the non-collisional nature of the shock, the tendency has been to use in priority the simplest fitting model available with least free parameters, that is, an empirical 2D polar equation (Russell, 1977; Slavin et al., 1991; J. Trotignon et al., 2006; Edberg et al., 2008; Hall et al., 2019). Only recently with the NASA/Mars Atmospheric and Volatile EvolutioN (MAVEN) mission were quadratic fits used to characterise the general structure of the Martian bow shock, with Gruesbeck et al. (2018) providing fits to a careful subset of identified crossings in the first year of operations of the MAVEN mission.

In recent years, many studies have attempted to characterise the Martian shock position and shape and its evolution under various solar wind and EUV conditions. Two missions have been used for this goal, the ESA/Mars Express mission and the NASA/MAVEN mission. Mars Express (hereafter MEX for brevity) was launched in 2003 and has been orbiting Mars since 2004, whereas MAVEN was launched ten years later in November 2013, and has been orbiting the planet since 22 September 2014. MAVEN's scientific payload includes among others a fluxgate magnetometer (MAG, Connerney et al., 2015), two ion spectrometers including the Solar Wind Ion Analyzer (SWIA, Halekas et al., 2015) and the Suprathermal and Thermal Ion Composition instrument (STATIC, McFadden et al., 2015), and an electron spectrometer (Solar Wind Electron Analyzer, SWEA, Mitchell et al., 2016). MEX unfortunately carries no magnetometer but includes an ion spectrometer suite called ASPERA-3 (Barabash et al., 2006), which was used to investigate the plasma boundaries at Mars (Dubinin et al., 2006). Both missions aim at studying the upper atmosphere and the magnetospheric environment of Mars.

We present in this study simple analytical algorithms using two types of historical fitting techniques (2D and 3D) in order to quickly estimate from spacecraft spatial coordinates the statistical geometrical position of the shock in planetary atmospheres. Special emphasis on the Martian environment is given throughout. This first crude estimator can be refined fur-

ther by applying additional criteria, for example on the magnetic field amplitude measured by the MAVEN spacecraft. This provides a fast means to approximately identify the position of the shock so that solar wind and magnetosheath/magnetosphere regions can be studied on a statistical level in the data. Moreover, other characteristics of the shock crossing, such as the quasi-parallel (noted $q_{\parallel}$) or quasi-perpendicular (noted $q_{\perp}$) nature of the shock can be easily obtained by deriving the perpendicular direction to the shock at any point on the surface. This is useful for specific studies where one of those regions needs to be excluded from the study (space weather-specific studies, for example), when areas around the predicted bow shock must be excluded for qualified reasons (this is the case for example if one wants to ignore foreshock and shock wake structures), or to approximately estimate the nature of the collisionless shock around the crossing.

After a review of 2D and 3D bow shock fitting models at Mars (Sect. 2), their leading equations and the elementary calculation of the normal to the bow shock at any point on the surface, the predictor algorithm for a fast estimation of the shock position in spacecraft orbital coordinates and its timing is presented. Refinement on the location of the shock in the data is also proposed with the sole help of magnetometer data (predictor-corrector algorithm). Application to the MAVEN MAG dataset is given as validation on a few examples and then extended to the whole available dataset. Finally, statistical analytical fits are given for the MAVEN mission between November 2014 and February 2021, with a discussion of the shock's asymmetry based on terminator and standoff distances. Applications for space weather-related databases are also mentioned.

2 Bow shock models at Mars

Martian bow shock 2D analytical shape models are sometimes given in aberrated solar wind coordinates in order to align the bow shock's major axis along the solar wind flow, which implicitly assumes axisymmetry along that axis. Formulae for analytical fits in 2D polar coordinates and 3D Cartesian coordinates are presented in this section. Calculations for the normal to the surface at a given point in space are also given, as a prolegomenon to the calculation of $q_{\perp} - q_{\parallel}$ shock conditions.

2.1 Coordinate systems and solar wind flow aberration

All spacecraft coordinates in this study are in Mars Solar Orbital coordinates (MSO) for simplicity, in accordance with most previous studies. In the MSO system, identical to the Sun-state coordinate system, the $+X_{\mathrm{MSO}}$ axis points towards the Sun from the planet's centre, $+Z_{\mathrm{MSO}}$ is towards Mars' North pole and perpendicular to the orbital plane defined as the X_{MSO}–Y_{MSO} plane passing through the centre of Mars, and Y_{MSO} completes the orthogonal system.

Because of the orbital motion of Mars with respect to the average direction of the solar wind, the apparent direction of the average solar wind in the rest frame of the planet deviates from the anti-sunward direction. As a result, an *anti-clockwise* rotation by an angle α around the Z axis must be applied so that the bow shock's main axis is aligned with respect to the X axis. This aberration, first seen in cometary tails and at the origin of the hypothesis by Biermann of a stellar wind (Biermann, 1951), is taken into account in the so-called *aberrated MSO coordinates*, denoted X'_{MSO}, Y'_{MSO} and Z'_{MSO} (although Z is left unchanged by the transformation). To unclutter notations, the 'MSO' subscript is now dropped. Following Formisano et al. (1979), Slavin and Holzer (1981) define the angle α as $\alpha = \tan^{-1}\left(V_{\mathrm{p}}/V_{\mathrm{sw}}\right)$ where V_{p} is Mars' orbital velocity and V_{sw} is the solar wind velocity, for example expressed in $\mathrm{km\,s^{-1}}$. The average orbital velocity is $V_{\mathrm{p}} = 24.07^{26.5}_{22.0}\ \mathrm{km\,s^{-1}}$. For the maximum value ($26.5\ \mathrm{km\,s^{-1}}$), the angle is $\alpha = 3.8°$ for a typical solar wind speed of $400\,\mathrm{km\,s^{-1}}$. The angle assumed by all studies except those of Slavin and Holzer (1981) and Slavin et al. (1991) is 4°. In Slavin and Holzer (1981), the aberration angle was chosen to be varying with solar wind speed conditions. In Slavin et al. (1991), $\alpha = 3.2°$. Figure 1 shows the aberration angle with respect to orbital velocity (abscissa) and to solar wind velocity (colour code).

2.2 Parametric models

Bow shock models at Mars have been proposed since the end of the 1970s, including (but not limited to): Russell (1977); Slavin and Holzer (1981); Slavin et al. (1991); Schwingenschuh et al. (1990); J. G. Trotignon et al. (1991); T.-L. Zhang, Schwingenschuh, Russell, and Luhmann (1991); T. L. Zhang, Schwingenschuh, Lichtenegger, et al. (1991); J. G. Trotignon et al. (1993); Vignes et al. (2000); J. Trotignon et al. (2006); Edberg et al. (2008, 2010). These studies were performed with several spacecraft including Viking, Mars Global Surveyor (MGS) and Phobos-2, and for varying solar conditions. In contrast with what was found at Venus, Slavin and Holzer (1981) and later Vignes et al. (2000, 2002) suggested that the mean bow shock stand-

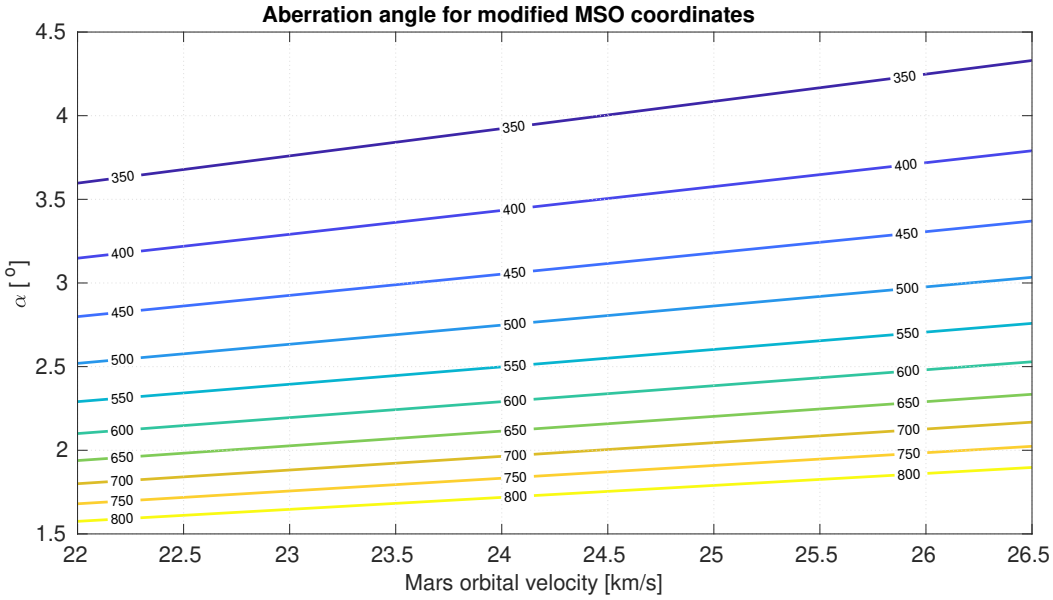

Figure 1. Aberration angle with respect to the orbital velocity of Mars (in km/s) and the solar wind mean speed (colour-coded isocontours, in km/s).

off distance is likely independent of the solar activity (using MGS and data from previous missions). Slavin et al. (1991) showed that the terminator distance, which is a marker of the swelling of the cavity flanks, varied by as much as 11% between the Mars-2,3,5 observations (low activity) and the Phobos-2 observations (high activity), although the number of crossings for each mission largely differed. MEX, with its very long activity spanning the end of solar cycle 23 and cycle 24 up to now (towards the beginning of new cycle 25), has the best chance to conclusively solve this aspect: Hall et al. (2019) found that for the years 2004–2017, the terminator distance shows variations up to ~ 7%, in agreement with J. G. Trotignon et al. (1993). Of note, Mazelle et al. (2004) made a review of all available measurements before MEX started observing, and discussed the solar cycle variations and the differences observed with Venus (for which up to 35% increase of the bow shock location in the terminator plane with increasing activity have been reported, see Russell et al., 1988; T. Zhang et al., 2008; Edberg et al., 2010).

Table 1 chronologically lists past bow shock studies and their characteristics in terms of solar activity, solar cycle number and number of observations, including the recent MEX and MAVEN surveys described in more detail below. Gringauz et al. (1976) quoted in Russell (1977) reported 11 crossings for the Russian Mars-2,3,5 satellites, but Slavin and Holzer (1981) later

reanalysed the datasets and found 14 crossings in total. Slavin et al. (1991) reported 94 crossings for Phobos-2, upped to 124 by J. G. Trotignon et al. (1993). For the entire period 2004–2015, Hall et al. (2016) identified 11,861 crossings in the MEX database. The more complete study in Hall et al. (2019) from 2004 to 2017 gathered 13,585 such crossings. Correspondingly, Ramstad et al. (2017) studied a subset of only 1,083 inbound and outbound MEX orbits for the period 2005 – 2016; they evaluated the dependence of the Ionosphere Boundary (IB), MPB and bow shock to EUV flux and solar wind lowest moments (density, bulk velocity). Of great import, Edberg et al. (2009, 2010) used MGS and MEX data in combination with ACE data extrapolated to Mars to study, among others, the dependence of the bow shock location to solar EUV flux and magnetosonic Mach number $M_{\rm ms}$. They pointed out that the shape of the magnetosonic shock wave depends on the ratio of the solar wind speed to the magnetosonic speed. Recently, Hall et al. (2016, 2019) made a statistical analysis of the bow shock position using MEX ion spectrometer data from 2004 to 2017 and used a standard 2D conic fit depending on the Martian Year (MY), with variations up to a few percent in terms of standoff bow shock distance. Simultaneously with MAVEN (both magnetometer and ion measurements), Halekas et al. (2017) investigated how the Martian magnetosphere and bow shock responded to EUV flux, $M_{\rm ms}$ and solar wind dynamic pressure between October 2014 and May 2016 (0.85 Martian year). In agreement with previous studies, they showed that the shock inflates with increasing EUV flux and contracts with increasing dynamic pressure and $M_{\rm ms}$; this in turn leads to EUV flux and dynamic pressure competing against one another because of their common $1/d_h^2$ dependence on heliocentric distance d_h.

As mentioned in the introduction, two approaches fitting the shape of bow shocks have been historically employed, one using a simple 2D polar form (e.g., Slavin & Holzer, 1981), the other the 3D general Cartesian conic form (e.g., Formisano et al., 1979; Formisano, 1979).

2.2.1 2D polar form

Assuming that a full-formed bow shock in aberrated coordinates is symmetric with respect to the X' axis, the 3D shape of the bow shock can be reduced to a 2D problem in the $(X',\ \sqrt{Y'^2 + Z'^2})$ plane. All Martian studies except that of Gruesbeck et al. (2018) have made this assumption. A simple 2D conic of revolution (usually a parabola or a hyperbola), symmetric around the aberrated MSO axis X' and decentred from its focus x_F is shown in Fig. 2.

Table 1. Statistical studies on the Martian bow shock location replaced chronologically (with respect to in-situ observations) in the context of solar activity and Martian Year (MY). N is the number of bow shock crossings considered in each study. MGS = Mars Global Surveyor. MEX = Mars Express.

Reference	Spacecraft	Years	N	Solar activity	Cycle #	Start	Max.	MY
Slavin and Holzer (1981)	Mariner 4	1965	2	*Low*	20	1964	1968	6
Russell (1977)[a]	Mars 2, 3, 5	1965 – 1974	11	*Low-Medium*	"	"	"	9 – 11
Slavin and Holzer (1981)	Mars 2, 3	1971 – 1972	10	*Medium*	"	"	"	9 – 10
Slavin and Holzer (1981)	Mars 5	1974	4	*Low*	"	"	"	11
Slavin et al. (1991)	Mar. 4, Mars 2, 3, 5	1965 – 1974	24	*Low-Medium*	"	"	"	6 – 11
Schwingenschuh et al. (1990)	Phobos 2	1989	~ 100	*High*	22	1986	1989	19
Slavin et al. (1991)	"	"	94	*High*	22	"	"	"
J. G. Trotignon et al. (1993)	"	"	26	"	"	"	"	"
J. G. Trotignon et al. (1993)[b]	"	"	126	"	"	"	"	"
Vignes et al. (2000)	MGS	1997 – 1998	450	*Low*	23	1996	2001	23 – 24
J. Trotignon et al. (2006)	MGS	09/1997 – 02/1999	573	*Low-Medium*	"	"	"	"
Edberg et al. (2008)	MGS	"	619	"	"	"	"	"
Hall et al. (2016)[c]	MEX	2004 – 2008	4,422	*Medium-Low*	"	"	"	27 – 29
Ramstad et al. (2017)[d]	MEX	11/2005 – 12/2016	2,166	*High-Medium*	23, 24	1996, 2008	2001, 2014	27 – 33
Hall et al. (2016)[e]	MEX	2008 – 2015	7,669	*Low-High*	24	2008	2014	30 – 32
Hall et al. (2019)[f]	MEX	2015 – 12/2017	1,494	*High-Medium*	"	"	"	33
Halekas et al. (2017)[g]	MAVEN	10/2014 – 05/2016	–	*High-Medium*	"	"	"	32 – 33
Gruesbeck et al. (2018)	MAVEN	11/2014 – 04/2017	1,799	*High-Medium*	"	"	"	32 – 34

[a] Observations by Gringauz et al. (1976) and analysed further by Russell (1977).
[b] In J. Trotignon et al. (2006), 127 Phobos 2 crossings of the bow shock were reported, that is, one more than in J. G. Trotignon et al. (1993).
[c] Data from Hall et al. (2019), MY27-29, Table 3 with respect to Martian Years. MY29 runs from 09-12-2007 to 25-10-2009, hence overlapping slightly with Solar Cycle 24, although still at minimum level of activity.
[d] About 7,000 orbits were first manually examined, "out of which 1,083 orbit inbound and outbound segments with identified BS, IMB or IB crossings were included." Orbital coverage of MEX is shown in their Fig. 9. No discrimination with solar cycle or Martian Year is given, although EUV flux and solar-wind parameter dependence are studied.
[e] Data from Hall et al. (2019), MY30-32, Table 3 with respect to Martian Years. MY32 runs from 31-07-2013 to 17-06-2015.
[f] Data from Hall et al. (2019), MY33, Table 3 with respect to Martian Years. MY33 runs from 18-06-2015 to 04-05-2017.
[g] Bow shock variations are obtained by fitting 2D-gridded datasets of average plasma density jumps through the shock location as measured with MAVEN/SWIA and are discriminated against M_{ms}, EUV flux and dynamic pressure.

Such a 2D conic takes the parametric form (for example, Hall et al., 2019):

$$r = \frac{L}{1 + \epsilon \cos\theta}, \tag{1}$$

$$\text{with: } r = \sqrt{(X' - x_F)^2 + Y'^2 + Z'^2}, \tag{2}$$

$$\text{and: } \cos\theta = \frac{X' - x_F}{r} \tag{3}$$

where θ is the angle measured from the focus of the conic (typically within the $[-\pi/2, \pi/2]$ range[1]), ϵ the conic's eccentricity, L the semilatus rectum (called *terminator crossing* by T. Zhang et al., 2008; Volwerk et al., 2016, at Venus, because the focus is taken at the centre of the planet). The equivalent rectangular (Cartesian) form of this equation is (J. Trotignon et al., 2006):

$$Y'^2 + Z'^2 - \left(\epsilon^2 - 1\right)(X' - x_F)^2 + 2\epsilon L (X' - x_F) - L^2 = 0. \tag{4}$$

In this representation, J. Trotignon et al. (2006) derived two additional useful quantities, the standoff shock distance along the X axis, R_{ss} (also called subsolar aerocentric distance in J. Trotignon

[1] This range of angles depends on the nature of the conic section. For a parabola, $\epsilon = 1$, and $\theta \in]-\pi, \pi[$ (borders excluded). For an ellipse, $\epsilon < 1$ and $\theta \in]-\pi, \pi]$. For a hyperbola, $\epsilon > 1$, and $\exists \theta_0 \in]0, \pi/2[\mid \cos\theta_0 = 1/\epsilon$, and $\theta \in]-\theta_0, \theta_0[\cup]\theta_0, 2\pi - \theta_0[$.

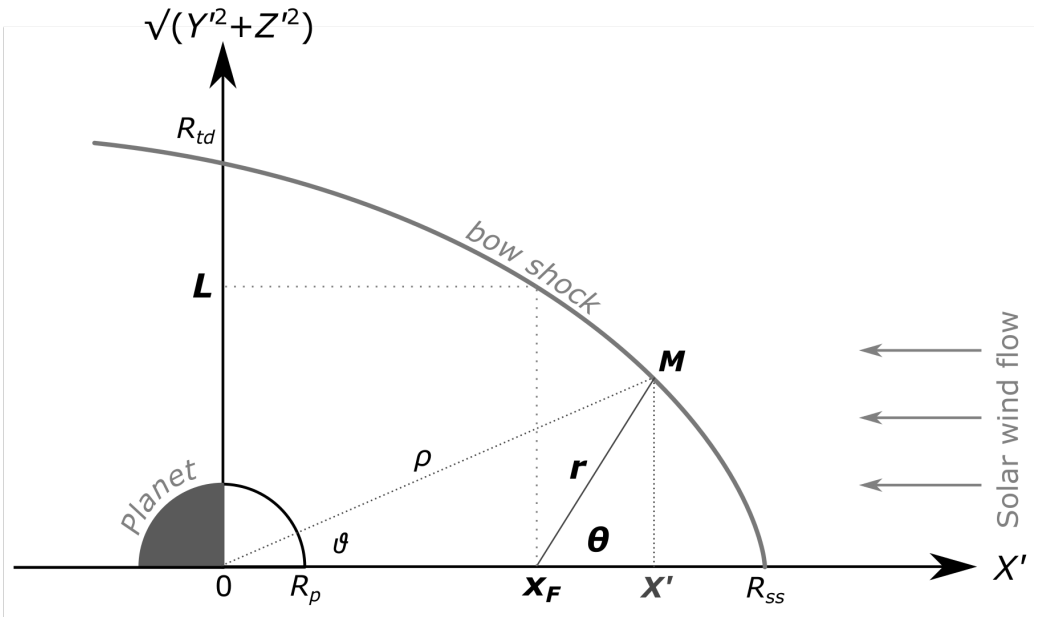

Figure 2. Typical 2D conic bow shock shape in the aberrated (X', $\sqrt{Y'^2 + Z'^2}$) coordinate system. For a point M on the shock surface, ρ is the Euclidean distance to the shock from the centre of the planet of radius R_p, and r is the distance to the shock surface from the focus x_F of the conic with semilatus rectum L and making an angle θ with the X' direction, so that Eq. (1) holds. ϑ is the usual polar angle, with respect to the centre of Mars. R_ss and R_td are the standoff subsolar and terminator distances.

et al., 2006) and the standoff terminator distance R_td along the cylindrical coordinate $\sqrt{Y'^2 + Z'^2}$ (which is none other than the diameter of the tail at $X' = 0$ divided by 2, or as in Russell, 1977, the "dawn radius"):

$$R_\mathrm{ss} = x_F + \frac{L}{1+\epsilon}, \tag{5}$$

$$R_\mathrm{td} = \sqrt{L^2 + (\epsilon^2 - 1)\, x_F^2 + 2\epsilon\, L\, x_F}. \tag{6}$$

Another parameter of interest can be derived, that is, the aperture of the Mach cone related to the shock structure –the *limiting Mach cone angle*. In gas dynamics theory it is defined as $\varrho = \sin^{-1} 1/M_\mathrm{ms}$, where $M_\mathrm{ms} = v_\mathrm{SW}/\sqrt{v_S^2 + v_A^2}$ is the magnetosonic Mach number. $v_S = \sqrt{\gamma P/\rho}$ is the sonic speed, whereas $v_A = B/\sqrt{\rho\mu_0}$ is the Alfvén speed, B the magnetic field intensity, ρ the solar wind ion mass density (typically with an admixture of 4% He^{2+} and 96% H^+). $\gamma = 5/3$ is the ratio of specific heats, and $P = n_\mathrm{sw}\, k_B(T_e + T_i)$ the solar wind thermal pressure, with T_e and T_i the electron and ion temperatures, respectively. For a hyperbola ($\epsilon >$

1), the limiting Mach cone angle is exactly the angle made by the asymptotes of the hyperbola (Slavin et al., 1984):

$$\varrho = \tan^{-1}\sqrt{\epsilon^2 - 1} \tag{7}$$

$$\text{with : } \Delta\varrho = \frac{\Delta\epsilon/\epsilon}{\sqrt{\epsilon^2 - 1}} \tag{8}$$

as uncertainty. In a canonical form for the hyperbola, with a the distance from the nose to the intersection of the asymptotes on the X' axis, and b that from the shock nose to the asymptote on the Y' axis, $\tan^{-1}\frac{b}{a}$. Since, by definition $\epsilon = \sqrt{1 + b^2/a^2}$, the substitution readily yields expression (7). It is noteworthy to remark that for ϵ close to 1, the uncertainty increases to infinity; any determination of ϱ is thus unreliable for quasi-parabolic curves.

For the fit, Slavin and Holzer (1981) and Slavin et al. (1991) rewrote Eq. (1) as $y = ax + b$ (posing $y = 1/r$, $x = \cos\theta$, $a = \epsilon/L$ and $b = 1/L$) and performed simple linear regressions for a range of foci locations. As pointed out by Vignes et al. (2000), this may result in fitting biases when observations are widely disparate in their location: in this case direct fitting methods to Eq. (1) should be preferred. With a direct polar fit to MGS data, Edberg et al. (2008) gave for example the following fitted values: $\epsilon = 1.05 \pm 0.04$, $L = 2.10 \pm 0.09$, $x_F = 0.55 \pm 0.12$. However, to match the results plotted in Fig. 1 of Edberg et al. (2008), the value of ϵ must be modified down to $\epsilon = 1.03$, a marginal difference likely due to rounding errors. For comparison, the corresponding values derived by Hall et al. (2019), for MEX data but with a larger sample, are $\epsilon = 0.998 \pm 0.003$, $L = 1.802 \pm 0.002$ and $x_F = 0.76$. For MGS and MEX data (Edberg et al., 2008; Hall et al., 2016, 2019), the subsolar standoff distance is $R_{ss} = 1.63 \pm 0.04\, R_p$, whereas the terminator standoff distance is $R_{td} = 2.50 \pm 0.09\, R_p$. By comparison, Halekas et al. (2017) found large variations of the bow shock standoff distances in the early MAVEN data, with $R_{ss} \sim 1.6$–$1.9\, R_p$ and $R_{td} \sim 2.5$–$3.1\, R_p$ depending on EUV flux levels and combined with either M_{ms} or the solar wind dynamic pressure. Differences towards upper values with previous studies likely stem from different EUV levels encountered by the respective missions which is one of the main drivers of the bow shock position (Halekas et al., 2017; Hall et al., 2019).

Table 2 presents for reference the fitted conic parameters of the main quoted references in Table 1, in chronological order. It is interesting to remark that most shapes fitted are *stricto sensu* hyperbolic ($\epsilon \geq 1$), but in practice can be considered quasi-parabolic as eccentricity $\epsilon \sim 1$, which makes it possible to calculate the limiting Mach cone angle. For example, when fitting bow shocks from different Martian years, Hall et al. (2019) showed that eccentricities

Table 2. Summary of Martian bow shock 2D conic parameters. Pre-Mars Express results were already summarised in J. Trotignon et al. (2006), Table 1. α is the aberration angle considered. ϱ is the limiting Mach cone angle, calculated by formula (7) in the case of a hyperbolic shape. The mean value for each mission is also given, with Mars 2-3-5 and Mariner 4 (Slavin et al., 1991), Phobos 2 (J. G. Trotignon et al., 1993), Mars Global Surveyor (MGS) (Edberg et al., 2008) and Mars Express (MEX) (with either Hall et al., 2016, 2019, for the calculation of ϱ). The planetary radius of Mars is by definition $R_\mathrm{p} = 3389.5$ km.

Reference	ϵ	L [R_p]	x_F [R_p]	R_ss [R_p]	R_td [R_p]	α	Nature	ϱ [°]
Russell (1977)[a]	0.99 ± 0.11	2.985	0	1.50 ± 0.15	3.00 ± 0.13	0	Ellipse	–
Slavin and Holzer (1981)[b]	0.94 ± 0.04	1.94 ± 0.02	0.5	1.50 ± 0.04	2.36[m]	$\tan^{-1}\frac{V_p}{V_\mathrm{sw}}$	Ellipse	–
Slavin et al. (1991)[c]	1.02	1.68	0.7	1.55	2.29[m]	$\tan^{-1}\frac{V_p}{V_\mathrm{sw}}$	Hyperbola	11.4 ± 2.9
Schwingenschuh et al. (1990)	0.85	2.72	0	1.47 ± 0.03	2.72[m]	3.8°	Ellipse	–
J. G. Trotignon et al. (1991)	0.95 ± 0.10	2.17 ± 0.03	0.5	1.62 ± 0.07	2.60[m]	4°	Ellipse	–
J. G. Trotignon et al. (1993)	1.02 ± 0.01	2.17 ± 0.03	0.5	1.57 ± 0.03	2.6	4°	Hyperbola	11.4 ± 2.8
Vignes et al. (2000)[d]	1.03 ± 0.01	2.04 ± 0.02	0.64 ± 0.02	1.64 ± 0.08	2.62 ± 0.09	4°	Hyperbola	13.9 ± 2.3
Vignes et al. (2000)[e]	1.02 ± 0.02	1.93 ± 0.01	0.72	1.67 ± 0.03	2.56 ± 0.06	4°	Hyperbola	11.4 ± 5.6
J. Trotignon et al. (2006)	1.026 ± 0.002	2.081 ± 0.006	0.6	1.63 ± 0.01	2.63 ± 0.01	4°	Hyperbola	12.9 ± 0.5
Edberg et al. (2008)[f]	1.05 ± 0.04	2.10 ± 0.09	0.55 ± 0.12	1.58 ± 0.18	2.69[m]	4°	Hyperbola	17.8 ± 6.8
Hall et al. (2016)	1.01 ± 0.11	1.82 ± 0.08	$0.74^{+0.03}_{-0.10}$	$1.65^{+0.13}_{-0.18}$	$2.46^{+0.20}_{-0.22}$	4°	Hyperbola	–[k]
Halekas et al. (2017)[g]	1.0	2.01–2.54	0.6	1.6–1.9[l]	2.5–3.1[m]	4°	Parabola	–
Ramstad et al. (2017)[h]	1.022	1.48	0.85	1.58	2.19	(4°)	Hyperbola	11.9 ± 2.7
Hall et al. (2019)[i]	0.998 ± 0.001	1.802 ± 0.002	0.76	1.662[l]	2.445 ± 0.003	4°	Ellipse	–
All (one per mission)[j]	1.016 ± 0.012	2.01 ± 0.25	0.61 ± 0.10	1.61 ± 0.08	2.56 ± 0.20	4°	Hyperbola	13 ± 4

[a] Because the Mars 2, 3 and 5 measurements reported by Gringauz et al. (1976) (in total 11 crossings) did not specify local times, aberration angle α was assumed to be zero.

[b] These authors use the full definition of the aberration angle, resulting in $\alpha = \tan^{-1}\frac{V_p}{V_\mathrm{sw}}$, in contrast to the more recent studies. See Sect. 2.1.

[c] Mariner 4, and Mars 2, 3, 5 data only here. Uncertainties on ϵ fitted values assumed to be 1%.

[d] "Direct fit" method with all 3 parameters varying simultaneously.

[e] "Slavin's method", using a linear regression in $(1/r, \cos\theta)$ space.

[f] Note that $\epsilon = 1.03$ matches better with Fig. 1 of Edberg et al. (2008), for which the Mach cone aperture would instead be $\varrho = 13.9$.

[g] Fits were performed on 2D-gridded density data, co-depending on M_ms and EUV flux levels on the one hand, and solar wind dynamic pressure and EUV flux levels on the other.
The coordinate system adopted by Halekas et al. (2017) was the Mars Solar Electric (MSE) system, with the X axis lying anti-parallel to the solar wind flow.

[h] Ramstad et al. (2017) use the following rectangular function (required to be cylindrically symmetric with respect to the solar wind direction):
$\rho = \sqrt{\epsilon^2 - 1}\,\sqrt{(x - R_\mathrm{ss} - \varsigma)^2 - \varsigma^2}$, with ρ the radial distance to the bow shock on the Y' axis from the centre of Mars, R_ss the subsolar standoff bow shock distance on the X' axis, and ς the so-called scale length. This function is valid $\forall x \neq R_\mathrm{ss}$ since $\rho(y = 0) = R_\mathrm{ss}$. By definition, $R_\mathrm{td} = \rho(x = 0) = \sqrt{\epsilon^2 - 1}\,\sqrt{(R_\mathrm{ss} + \varsigma)^2 - \varsigma^2}$.
ς is a constant equal to $33.54\,R_\mathrm{p}$ derived in Ramstad et al. (2017) from the bow shock model values for R_ss, R_td and ϵ of Vignes et al. (2000) and can be calculated as $\varsigma = -\frac{1}{2R_\mathrm{ss}}\left(R_\mathrm{ss}^2 - R_\mathrm{td}^2/(\epsilon^2 - 1)\right)$. The original values of R_ss and ϵ in their study were fitted to a function $a\,n_\mathrm{sw}^b\,(v_\mathrm{sw}/100)^c + d$; we have assumed here nominal conditions $(n_\mathrm{sw}, v_\mathrm{sw}) = (2\,\mathrm{cm}^{-3}, 400\,\mathrm{km\,s}^{-1})$ for simplicity. We calculate the semilatus rectum as $L = \left(R_\mathrm{td}^2 - (\epsilon^2 - 1)R_\mathrm{ss}^2\right)/(2R_\mathrm{ss})$ from formulae (5) and (6). Uncertainties on ϵ fitted values assumed to be 1%.

[i] Here we only recall the results for all MYs (MY27 – 33). Individual MYs have eccentricities below 1 (ellipse), except for MY28 – 29 (hyperbola).

[j] That is, Mariner 4 and Mars 2-3-5 (Slavin et al., 1991), Phobos 2 (J. G. Trotignon et al., 1993), MGS (Edberg et al., 2008), MEX (Hall et al., 2019) and MAVEN (Halekas et al., 2017). The listed uncertainties are the standard deviations of the series. Accordingly mean angles ϱ are calculated only for 3 values and are only given for for completeness here.

[k] Although this is a hyperbola with cone angle $\varrho = 8.1°$, the large eccentricity uncertainty leads to a cone angle uncertainty of 44°, hence no ϱ value is provided here.

[l] Calculated from formula (5).

[m] Calculated from formula (6).

varied around $\epsilon = 1$ by less than 5% between Mars Year 27 (MY27) and MY33, with a marked tendency towards ellipsoidal shapes (only 2 consecutive years, MY28 and MY29 had eccentricities above 1).

2.2.2 3D Cartesian form

The more general way of characterising the bow shock shape does not assume any symmetry with respect to any axis. A 3D shape model can be constructed in the form of a quadratic

equation (for example, Formisano et al., 1979; Gruesbeck et al., 2018; Simon Wedlund et al., 2017, for Earth, Mars and comets):

$$Ax^2 + By^2 + Cz^2 + Dxy + Eyz + Fxz + Gx + Hy + Iz - 1 = 0. \tag{9}$$

Here and for clarity in the equations, (x, y, z) coordinates are by definition the unaberrated $(X_{\mathrm{MSO}}, Y_{\mathrm{MSO}}, Z_{\mathrm{MSO}})$ coordinates. With the MAVEN spacecraft including both magnetometer and ion spectrometer, Gruesbeck et al. (2018) used a limited subset of bow shock crossings when ignoring rapid spatial motions of the boundary across the spacecraft due to the variable solar wind (see Halekas et al., 2017), leaving a database of only 1799 crossings spanning about 3 years of data (November 2014 to April 2017). For all bow shock detections considered in their study, the best least-squares ellipsoid fit was obtained with $A = 0.049$, $B = 0.157$, $C = 0.153$, $D = 0.026$, $E = 0.012$, $F = 0.051$, $G = 0.566$, $H = -0.031$, $I = 0.019$ and is valid only for the dayside bow shock up to a few $0.1\,R_{\mathrm{p}}$ downstream of the terminator ($X' \gtrsim -0.5\,R_{\mathrm{p}}$) because of the poor MAVEN orbital coverage on the nightside flanks of the shock[2]. Gruesbeck et al. (2018) concluded that asymmetry of the shock surface was particularly pronounced in the North-South direction due to the influence of crustal magnetic field anomalies. Located predominantly in the southern hemisphere of Mars between 30°S−85°S, they tend to increase the altitude of the induced magnetospheric boundary and hence increase the subsolar standoff distance.

Although quadratic surfaces are not necessarily centered on the planet nor is their main axis directed along the X_{MSO} axis (see Appendix Appendix A), a simple estimate of the shock's position in the subsolar and terminator directions can be of interest. From Eq. (9), a subsolar standoff distance along the X_{MSO} axis can be derived at coordinates $(x,\ y = 0,\ z = 0)$ by finding the positive root of the simplified quadratic equation (i.e., the intersection of the surface with the X_{MSO} axis):

$$Ax^2 + Gx - 1 = 0 \tag{10}$$

$$\implies x_{\mathrm{max}} = R_{\mathrm{ss}} = \frac{-G + \sqrt{G^2 + 4A}}{2A}, \tag{11}$$

[2] This is the downside of having regular "deep dips" and a much better ionospheric coverage; the inclination and eccentricity of the orbit of MAVEN have never been too favourable to exploring those regions.

whereas the terminator standoff distances in the $Y-Z$ plane (non-aberrated MSO coordinates) are similarly given by:

$$By^2 + Hy - 1 = 0 \quad \Longrightarrow \quad y_{\max} = R_{\mathrm{td},y} = \frac{-H + \sqrt{H^2 + 4B}}{2B} \tag{12}$$

$$Cz^2 + Iz - 1 = 0 \quad \Longrightarrow \quad z_{\max} = R_{\mathrm{td},z} = \frac{-I + \sqrt{I^2 + 4C}}{2C} \tag{13}$$

Because of the small angles involved at Mars, non-aberrated coordinates are rather accurate for the subsolar standoff distance. That said, rotating the MSO coordinate system by a certain small angle α about the Z axis does impact the terminator distances by a few $0.01\,R_{\mathrm{p}}$. For the parameters given above, $R_{\mathrm{ss}} = 1.56\,R_{\mathrm{p}}$, $R_{\mathrm{td},z} = 2.50\,R_{\mathrm{p}}$ and $R_{\mathrm{td},y} = 2.62\,R_{\mathrm{p}}$. Because the shock is a 3D object, the exact position of the tip of the ellipsoid may vary with respect to the values taken at the origin.

2.2.3 Comparison of historical models

A comparison of a representative selection of historical bow shock models (some of them as listed in Vignes et al., 2000; J. Trotignon et al., 2006) in the $X'-Y'/Z'$ plane is given in Fig. 3. For ease of comparison, the 3D quadratic model of Gruesbeck et al. (2018) was rotated anticlockwise by 4° around the Z axis. It is noteworthy to remark that although the fit is not valid for $X' \lesssim -0.5\,R_{\mathrm{p}}$, the figure displays the fits for $X' > -2.5\,R_{\mathrm{p}}$ to illustrate the differences in shock surface swelling.

All models are in excellent agreement around the subsolar point, with a mean subsolar standoff distance value of $R_{\mathrm{ss}} = 1.59 \pm 0.05\,R_{\mathrm{p}}$. The terminator standoff distance is also in very good agreement – however, for $X' \lesssim 0\,R_{\mathrm{p}}$, the difference between fits becomes substantial, especially (*i*) between the recent MEX investigations of Hall et al. (2016, 2019) and the other fits on the one hand, and (*ii*) between the MAVEN fits and the other fits on the other. For MAVEN, this is due, as previously mentioned, to the lack of orbit sampling by the spacecraft for $X' < 0\,R_{\mathrm{p}}$. In this sense, MEX has a much better antisolar spatial coverage. The North-South asymmetry in the 3D fits of Gruesbeck et al. (2018) can be easily seen, a characteristic which no axisymmetric model can directly quantify.

2.3 Nature of the shock

2.3.1 Quasi-perpendicular or quasi-parallel shock?

A collisionless shock may have different behaviours depending on the upstream solar wind magnetic field (the IMF), which conditions how the solar wind is losing its energy to the magnetosheath. Two main cases are conveniently studied for their varying properties: $q_{\parallel}$ and $q_{\perp}$ shocks. Additional important physical quantities driving the shock structure and dynamics are the magnetosonic Mach number (which defines the shock's criticality) and the plasma-β (Balogh & Treumann, 2013).

It is useful to recall that a $q_{\parallel}$ shock condition is defined so that the background IMF lines are intersecting normally the shock surface, whereas a $q_{\perp}$ shock describes an IMF that is in effect *in the tangent plane* to the surface shock. Thus, the angle of importance is the angle between the average IMF vector upstream of the shock and the shock normal. This angle is in the literature almost always named θ_{Bn}, which is kept here for convenience. The nature of the shock is defined as follows:

$$\theta_{Bn} > 45^{\circ} : q_{\perp} \text{ shock} \tag{14}$$

$$\theta_{Bn} \leq 45^{\circ} : q_{\parallel} \text{ shock} \tag{15}$$

Starting in the magnetic field compression region in the solar wind, $q_{\perp}$ shocks have structures, from the point of view of B-fields, almost always characterised by (*i*) a foot, (*ii*) a fast ramp, and (*iii*) a wider overshoot followed by a more gradual undershoot (see Kennel et al., 1985, Fig. 11). This classic picture is a first approximation as fine electron-scale structures in the foreshock, foot and ramp can be seen with high-cadence magnetic field measurements. $Q_{\perp}$ shocks reflect particles back upstream to satisfy the shock conditions and are on average diffusive. Magnetic structures trapping particles such as mirror modes are observed to predominantly take place in the magnetosheath behind a $q_{\perp}$ shock (Gary, 1992). On the other hand, $q_{\parallel}$ shocks are on average resistive and are usually characterised by heavy turbulence. Their foreshock contains MHD turbulence that can give rise to first-order Fermi acceleration. Also common in the foreshock region, highly compressive structures such as Short Large-Amplitude Magnetic Structures (SLAMS) are associated to large density variations: they originate from the steepening of ULF waves and are of great importance in the shock reformation (Burgess et al., 2005; Burgess & Scholer, 2014).

In order to determine whether the $q_{\parallel}$ or $q_{\perp}$ nature of the shock is crossed by a spacecraft, the normal direction to the shock surface needs to be first estimated. For a single spacecraft, this can be estimated either with methods that take advantage of upstream and downstream magnetic field measurements (coplanarity method as in Horbury et al., 2002, although prone to rather large uncertainties) or through geometrical considerations only, as shown below. The magnetic coplanarity method is expounded for example in Schwartz (1998), and compares upstream and downstream average fields to calculate with the vectorial product the local normal to the shock boundary. The accuracy of the geometrical method shown below is linked to the assumption that the shock surface is smooth and does not possess any kinks or local structures where the current curls on itself. In practice this is not the case and the shock may assume a more rippled shape which depends on the upstream solar wind condition and the turbulence at the boundary (Moullard et al., 2006). However, this geometric determination may still be a useful first approximation of the nature of the shock.

2.3.2 Determination of the shock normal

The normal to the shock surface at point (r_0, θ_0) in polar coordinates, (x_0, y_0, z_0) in Cartesian coordinates or $(r_0, \vartheta_0, \varphi_0)$ in spherical coordinates is simply defined as the gradient vector of the (assumed) smooth surface f at that point. Mathematically this is expressed as:

$$\nabla f \cdot \mathbf{v} = 0 \tag{16}$$

where $\mathbf{v}$ is a vector tangential to the surface at that point.

2D case. For the 2D polar coordinate case, let f be equal to $f(r, \theta) = r - L/(1+\epsilon\cos\theta)$ following Eq. (1) where θ is the angle from the focus x_F on the X' axis. The gradient of f depends on the two variables (r, θ):

$$\nabla f = \begin{pmatrix} \frac{\partial f}{\partial r} \\ \frac{1}{r}\frac{\partial f}{\partial \theta} \end{pmatrix} = \begin{pmatrix} 1 \\ -\frac{\epsilon \sin\theta}{(1+\epsilon\cos\theta)} \end{pmatrix} \tag{17}$$

At point (r_0, θ_0) vector $\nabla f = (R_0, \Theta_0)$ is perpendicular to the surface. Note that because of the peculiarity of a conic, values in x must always be corrected by the focus distance x_F, because the typical polar angle ϑ is not strictly the same as the conic angle θ used in Eq. (1) (see Fig. 2).

In Cartesian coordinates, using Eq. (4), the gradient will be against directions along X' and Y' and equal to:

$$\nabla f = \begin{pmatrix} \frac{\partial f}{\partial X'} \\ \frac{\partial f}{\partial Y'} \end{pmatrix} = \begin{pmatrix} -2\left(\epsilon^2 - 1\right)(X' - x_F) + 2\epsilon L \\ 2Y' \end{pmatrix}. \tag{18}$$

This expression circumvents the ambiguity on the angle direction of the polar formula, and is thus privileged when calculating the normal direction. Figure 4 (left) displays the normal direction to several points on the shock surface as calculated by this technique applied to the 2D bow shock polar fit of Edberg et al. (2008), and converted to Cartesian coordinates.

3D case. For the 3D Cartesian quadratic equation, f is simply equal to the left member of equation (9).

The gradient of f is then simply:

$$\nabla f = \begin{pmatrix} \frac{\partial f}{\partial x} \\ \frac{\partial f}{\partial y} \\ \frac{\partial f}{\partial z} \end{pmatrix} = \begin{pmatrix} 2Ax + Dy + Fz + G \\ Dx + 2By + Ez + H \\ Fx + Ey + 2Cz + I \end{pmatrix} \tag{19}$$

At point (x_0, y_0, z_0) vector $\nabla f = (X_0, Y_0, Z_0)$ is perpendicular to the surface. The equation of the tangent plane to the smooth surface at that point is of the general form:

$$\left.\frac{\partial f}{\partial x}\right|_0 (x - x_0) + \left.\frac{\partial f}{\partial y}\right|_0 (y - y_0) + \left.\frac{\partial f}{\partial z}\right|_0 (z - z_0) = 0, \tag{20}$$

where subscript "0" in the gradient components denotes the gradient taken at points (x_0, y_0, z_0) for brevity. Thus, knowing the 3D position of the spacecraft at the expected bow shock position, one can calculate the transverse and tangent directions to the bow shock surface.

Figure 4 (right) shows this technique applied to the 3D bow shock fit of Gruesbeck et al. (2018), assuming a spacecraft situated on random points of the shock's surface.

Calculating the angle θ_{Bn} from the average direction of the magnetic field then becomes trivial, in a geometric sense. Because of the inherent 3D nature of a spacecraft orbit and of the local magnetic field, the 3D calculation of Eq. (19) is usually preferred to the 2D case (Eq. 18). It is however important to recall here that the shock's local shape may be assuming that of a "corrugated iron" section, as it was evidenced for example at Earth with the Cluster quartet of spacecraft (Moullard et al., 2006). No method is foolproof in estimating θ_{Bn}: the local normal to the shock must then be more carefully checked for each specific event, for which several complementary methods do exist, such as the magnetic coplanarity method.

When applied to the MAVEN dataset, the geometric calculation of θ_{Bn}, always assuming a smooth surface, is expected to reach an uncertainty of about $\pm 5°$ depending on the upstream field determination. This estimate was obtained for a small sample of crossings by extending over a few minutes the time spans used to calculate the upstream magnetic field direction.

3 Detecting the bow shock in spacecraft orbits

Estimating the bow shock position from spacecraft spatial coordinates can be achieved either empirically or theoretically, depending on the precision needed. Semi-empirical but computationally intensive techniques using machine-learning imaging algorithms are currently attempted to detect automatically and precisely the exact position of the shock from the full plasma instrumental payload on board planetary missions. However, a faster approach, based on a simple geometrical estimator using a static analytical bow shock model (see Sect. 2), may still prove valuable for statistical studies or for new datasets. Such an approach and its possible refinements in 2D and 3D coordinate systems based on magnetic field-only measurements are presented below.

3.1 Predictor algorithm for the shock position from previous analytical models

2D case. In the 2D polar conic model, one angle θ unequivocally defines the distance r from the focus of the conic to the bow shock. Comparing the corresponding spacecraft Euclidean distance with r at each spacecraft location defined by θ makes it possible to determine if the spacecraft is *in-* or *outside* of the shock surface. The algorithm is the following (see Fig. 2 for definitions of angle and distances):

- Calculate the spacecraft's Euclidean distance from the chosen conic model focus x_F, in aberrated MSO coordinates, so that: $r_{\rm sc} = \sqrt{(X'_{\rm sc} - x_F)^2 + Y'^2_{\rm sc} + Z'^2_{\rm sc}}$,
- Calculate the angle θ at position of the spacecraft: $\theta = \arctan \sqrt{Y'^2_{\rm sc} + Z'^2_{\rm sc}} / (X'_{\rm sc} - x_F)$,
- Calculate the bow shock distance $R_{\rm bs}$ at the corresponding spacecraft θ angle from the focus x_F: $R_{\rm bs} = L/(1 + \epsilon \cos\theta)$ following Eq. (1),
- Compare $R_{\rm bs}$ and $r_{\rm sc}$.

This approach was tested for polar coordinate models (such as Edberg et al., 2008; Hall et al., 2016, 2019) provided that all spacecraft coordinates are first rotated 4° into the aberrated MSO system.

3D case. For 3D quadric models (Gruesbeck et al., 2018), the aberration is already taken into account and there is no need to correct the spacecraft coordinates for the position of the focus of the conic. Thus we only need generalise the approach above to spherical coordinates $(\rho, \vartheta, \varphi)$, where $\rho = \sqrt{X^2 + Y^2 + Z^2}$ is the planetocentric distance, whereas $\vartheta = \arctan Y/X$ and $\varphi = \arctan Z/\sqrt{X^2 + Y^2}$ represent azimuth and elevation by convention. To compensate for the inherent ambiguity on azimuth depending on the quadrant, the function $\arctan 2$ is preferred throughout. Equation (9) becomes a second-degree equation of the form:

$$a\rho^2 + b\rho - 1 = 0 \tag{21}$$

with:

$$a = A\cos^2\varphi\,\cos^2\vartheta + B\cos^2\varphi\,\sin^2\vartheta + C\sin^2\varphi + \frac{D}{2}\cos^2\varphi\,\sin 2\vartheta + \frac{E}{2}\,\sin 2\varphi\,\sin\vartheta + \frac{F}{2}\,\sin 2\varphi\,\cos\vartheta$$

and:

$$b = G\cos\varphi\,\cos\vartheta + H\cos\varphi\,\sin\vartheta + I\sin\varphi$$

In the case of an ellipsoid of revolution (as it is the case for the parametrisation of Gruesbeck et al., 2018), the bow shock distance R_{bs} at the angles (ϑ,φ) corresponds to the positive root of this equation:

$$R_{\mathrm{bs}} = \frac{-b + \sqrt{4a + b^2}}{2a}, \tag{22}$$

for $a \neq 0$. For other parametrisations such as a hyperboloid of two sheets, there may be two positive roots, in which case the smallest root should be chosen.

The denominator $2a$ in expression (22) never reaches zero, no matter the combination of angles chosen, which makes it a robust formula throughout any orbit. For azimuth and elevation angles ($|\vartheta| \gtrsim 115°, |\varphi| \lesssim 55°$), the model of Gruesbeck et al. (2018) is not applicable any more (standoff distances above $4\,R_{\mathrm{p}}$) as these particular angular combination corresponds to a tail-flank position, which was outside of MAVEN's orbital range.

The next step is to determine whether the spacecraft is inside the bow shock surface or outside of it in the orbital sequence. The algorithm follows a similar sequence as for the 2D

case, but all variables are calculated with respect to the centre of Mars, in unaberrated MSO coordinates:

- Calculate the spacecraft's Euclidean distance in non-aberrated coordinates, $R_{\rm sc} = \sqrt{X_{\rm sc}^2 + Y_{\rm sc}^2 + Z_{\rm sc}^2}$,
- Calculate (azimuth, elevation) angles (ϑ, φ) at position of the spacecraft so that: $\vartheta = \arctan \frac{Y_{\rm sc}}{X_{\rm sc}}$ and $\varphi = \arctan \frac{Z_{\rm sc}}{\sqrt{X_{\rm sc}^2 + Y_{\rm sc}^2}}$,
- Calculate the bow shock distance $R_{\rm bs}$ at the corresponding spacecraft spherical angles with Eq. (22),
- Compare $R_{\rm bs}$ and $R_{\rm sc}$.

Using 1-min-averaged MAVEN orbits, the automatic detection of the bow shock is performed and shown in Fig. 5. Because of the relatively poor temporal resolution of this dataset, as well as the fast approach in the early stages of the orbit insertion, some points in the orbit yield false positive detections which disappear when increasing the orbital resolution to 1 s.

Thanks to the simple algorithms presented above, bow shock crossings may be statistically predicted in a given spacecraft orbit. To help identify the solar wind region, distinction can be made between trajectories moving from the magnetosheath to the solar wind region, and vice-versa. For each orbit intersecting the bow shock model, two points per orbit will be identified. At 1 s resolution, a total of 16,515 bow shock crossings using the 3D analytical model of Gruesbeck et al. (2018) were predicted for the MAVEN dataset between November 2014 and February 2021, including 8,256 crossings from the sheath to the solar wind and 8,259 crossings from the solar wind to the sheath.

Actual crossings will in practice be different and the algorithms may fail to pinpoint the location of the shock sometimes by several tens of minutes, mostly because of solar wind varying conditions, or due to the nature of the shock at the point of passage for an individual orbit (Halekas et al., 2017). We estimate thus the precision of these automatic estimates to be of the order of $\pm 0.08\, R_p$ (± 270 km) around the 'true' bow shock location. Because of variable shock position from orbit to orbit and the geometric average nature of the detection, some orbits that may have experienced shock crossings but lie inside the average shock position will not be tested for potential detection. It is estimated that only a few hundred potential crossings were ignored in the process. Consequently, the true shock structure location should be checked directly in the magnetic field and ion data. Moreover, since the bow shock is a dynamical object, it may experience fast forward and backward motions, crossing the spacecraft

trajectory several times more per orbit. This can be seen for example in Fig. 6, third panel, where the total magnetic field undergoes sharp intermittent jumps in the foreshock area (22 June 2018, around 01:00 UT).

This 3D algorithm was successfully applied to the retrieval of undisturbed solar wind density and velocity moments in the MAVEN/SWIA data with 1 min resolution, as part of the Helio4Cast solar wind in-situ data cataloguing enabling the statistical study of interplanetary coronal mass ejections and high speed streams (Möstl et al., 2020).

3.2 Refining the position of the shock: a predictor-corrector approach

Because of variations in the shock position, the automatic detection may give inaccurate predictions. A fast method to correct to a certain extent for these discrepancies is presented here. It makes use of the magnitude of **B** to identify the position of the shock structure, either when crossing from the magnetosheath into the solar wind or vice-versa. As before, the main assumption is that the shock is crossed twice per orbit at maximum, although in practice the shock structure may be crossed several times due to the fast motion of the boundary across the spacecraft trajectory (Halekas et al., 2017). Because we are interested in the statistical position of the shock, this assumption nonetheless provides a valuable estimate of the average position of the shock during those times. All magnetic field data are assumed here to be of the order of 1-s resolution. Because of the clear signature of $q_\perp$ crossings (with a sharp B-field ramp) as compared to $q_\parallel$ crossings, this method is biased towards the detection of $q_\perp$ crossings.

The predictor-corrector detection algorithm attempts to consistently identify solar wind undisturbed regions in the chosen dataset, and proceeds as follows:

1. Calculate predictor estimate of the shock's timing $t_{\rm sh}$ with the automatic algorithm in 2D aberrated polar coordinates or in 3D (Sect. 3.1),
2. Choose a **B**-field data time interval around the estimated shock so that $[t_{\rm sh}-\Delta t_{\rm sh}, t_{\rm sh}+\Delta t_{\rm sh}]$,
3. Calculate a robust estimate of the average magnetic field, e.g., the median of the magnetic field $|B_{\rm sw}|_{1/2}$, in half of this interval (hence the subscript). By definition $|B_{\rm sw}|_{1/2}$ corresponds to the assumed solar wind region. For crossings from the sheath to the solar wind, the second half of the interval is selected. For crossings from the solar wind

into the sheath, the first half interval is selected. There are two possibilities at this junction:

(a) If $|B_{sw}|_{1/2} > B_{th}$, where B_{th} is the solar wind-to-magnetosheath threshold, the position of the solar wind region is difficult to assess. In that case:

   i. Make the time interval float around the estimated location of the shock, by increments of $\Delta t_{sh}/3$ in one direction or the other, regardless,

   ii. Repeat interval shift until $|B_{sw}|_{1/2} \leq B_{th}$ or until a maximum shift of $2\Delta t_{sh}$ is effected from the estimated shock timing in either direction. If $|B_{sw}|_{1/2}$ is still greater than B_{th}, the crossing is altogether ignored and removed from the database.

(b) If $|B_{sw}|_{1/2} \leq B_{th}$, the undisturbed solar wind seems to be clearly identifiable in the data. In that case:

   i. Calculate the running Median Absolute Deviation (MAD) $\varsigma_{mad,B}$ of the signal over a temporal width of duration T in the chosen interval, and smooth further the result with a running median over a time span enclosing the shock structure in its entirety (for example $2T$ or $3T$). This also helps remove potentially abrupt but temporally isolated changes in the signal. Note that this particular choice of $\varsigma_{mad,B}$ is somewhat arbitrary. After several tests including running standard deviations, normalised or not to the "solar wind" signal, the choice of a smoothed running MAD was empirically found to work consistently well with the MAVEN dataset at 1 s resolution.

   ii. Compare $\varsigma_{mad,B}$ to threshold value ς_{th}. A jump above a certain threshold ς_{th} indicates a transition between a less turbulent region to a more turbulent one, an indicator of the presence of a shock-like structure. If this threshold is reached, take the first (respectively, last) time this happens in the chosen interval for solar wind-to-sheath (respectively, sheath-to-solar wind) crossings, and correct the original timing of step 1. If not, discard crossing.

At Mars, step 1 (predictor) was tested in the previous section for the MAVEN dataset: on average, the detected shock was within $\pm 0.08\,R_p$ (± 270 km) of the true shock crossing, corresponding to about $\Delta t_{sh} \pm 30$ min of data along the orbit.

The typical threshold values used for the MAVEN mission were determined manually, for simplicity, on a reduced dataset. A good compromise was found by trial and error with $B_{th} = 11$ nT, because the undisturbed solar wind magnetic field in Mars' vicinity is of the

order of 2−5 nT on average (Slavin & Holzer, 1981), but can reach up to about 10 nT when solar transient effects such as coronal mass ejections or co-rotating interaction regions are involved (Liu et al., 2021). In future studies, a more dynamic criterion in step (3a) may be preferred, i.e., where the level of the B-field is normalised to the assumed upstream solar wind value. The criterion for a clear magnetosheath could for example become $\gamma = |B|/|B_{\rm sw}|_{1/2} > \gamma_{\rm th}$, where $\gamma_{\rm th}$ is an adequately chosen threshold ($\gamma \sim 1.5$ for a clear increase of magnetic field when moving into the magnetosheath, with nominal solar wind levels $\gamma \sim 1$).

Because the shock appears in measurements as a turbulent structure whereas the solar wind is on average less so, step (3b-i) calculates a measure of the variability of the magnetic field in the vicinity of the shock. When in the solar wind, the intrinsic variability of the signal $\varsigma_{\rm mad,B}$ is on average found to be less than 0.5, which is adopted as the threshold $\varsigma_{\rm th}$. This makes it possible to detect the very first perturbations in the solar wind leading to the creation of the shock structure, a point which is identified here as the position of the shock proper at time $t_{\rm sh}$. Again, in future studies, the threshold can be normalised to the magnetic field level, as in Halekas et al. (2017) where, together with constraints on plasma parameters, the normalised root-sum-squared value of the magnetic field was chosen so that $\mathrm{RSS}_B/\mathbf{B} < 0.15$ to identify undisturbed solar wind intervals.

Applied to the MAVEN dataset at 1-s orbital and magnetic field resolution, the corrector algorithm reaches an accuracy of $\pm 0.02\,R_p$ (± 70 km) around the true shock, a factor 4 increase in accuracy with respect to step 1. In the temporal datasets, this corresponds to only a few minutes of continuous data along MAVEN's orbit. This is epitomised in Fig. 6, which presents examples of bow shock crossings around Mars as seen with the MAG instrument on board MAVEN throughout the mission. Corrections to the location with the above predictor-corrector algorithm are shown as unbroken lines whereas step 1 predictions are in dashed lines.

At the beginning of the mission (Fig. 6, upper panel, Dec. 2014), the automatic predictor algorithm gives a reliable estimate of this $q_\perp$ shock's position: this is expected since the prediction is based on the 3D quadric model of Gruesbeck et al. (2018) who specifically performed shock fits on the first years of the mission. In this case, the predictor-corrector algorithm only corrects the shock's estimated location by a few minutes. The second panel of Fig. 6 (Sept. 2016) displays a case where the shock position is hard to ascertain from magnetic-field data only: the predictor estimate is off by up to 20 minutes for all crossings. Because of the constraints on the magnetic field amplitude and the lack of significant variations in $|B|$ between

22:00 and 01:00 UT, the predictor-corrector algorithm ignores the two first expected crossings but corrects well for the two next crossings (around 03:30 and 04:45 UT). Figure 6's third panel shows a more complex mix between sheath and solar wind conditions, and even though the boundaries are more subtle and the overall B-field magnitude below 10 nT, the predictor-corrector algorithm manages to estimate well the position of the $q_{\parallel}$ shock, ignoring potential crossings which do not fulfil the stringent threshold condition on $\varsigma_{\mathrm{mad,B}}$. Multiple bow shock crossings can be seen, especially for the discarded potential crossings from solar wind to magnetosheath around 01:00 UT, or later around 06:00 UT. The bottom panel shows yet another example of the superiority of the predictor-corrector algorithm when it comes to very clear bow shock crossings in 2020, after the orbit of MAVEN had been altered into a different orbit than at the beginning of the mission.

The final corrected timings for the detections yield with this algorithm a lower estimate of the total actual number of crossings encountered by a spacecraft throughout its mission. Events occurring when $|B_{\mathrm{sw}}|_{1/2} > B_{\mathrm{th}}$, even after shifting the temporal window significantly, or when $\varsigma_{\mathrm{mad,B}} < \varsigma_{\mathrm{th}}$, were discarded in the final selection as can be seen in Fig. 6. They may indicate that the magnetic field was either too turbulent or too complex in its structure (e.g., multiple crossings as is regularly the case with $q_{\parallel}$ crossings) for the corrector algorithm to capture. Moreover, as discussed previously, the analytical approximation model used for the determination in step 1 (either 2D or 3D) is likely to underestimate the true number of crossings due to the planetary bow shock variability (Halekas et al., 2017). Because our study is primarily interested in the statistical position of the bow shock throughout the mission, this loss of potential detections may be compensated by the large number of orbits of the considered spacecraft.

For MAVEN, from the original 16,515 candidate detections from step 1 (predictor) using the 3D model of Gruesbeck et al. (2018) as a first approximation, the predictor-corrector algorithm selected 14,929 events (7,494 detections from the solar wind to the magnetosheath and 7,435 from the sheath to the solar wind) for the period 01 November 2014 to 07 February 2021. This is a 10% decrease in number of crossings, leaving out the less ambiguous events of the geometric detection only. On average, the correction to the original timing is within about $\Delta t \pm 20$ min along the spacecraft orbit, which corresponds to a percentage difference in radial distance of about ±25% (not shown). The calculated average difference $|\Delta R_{bs}|$ over the entire dataset between predictor and predictor-corrector algorithm is $\sim 0.11\,R_p$, i.e., ~ 380 km or about 5% difference.

Out of these 14,929 crossings, an overwhelming number (11,967) was found to be predominantly $q_\perp$ crossings with $\theta_{Bn} > 45°$ as calculated with formula (19), the remaining 2,962 events being classified as more reminiscent of $q_\parallel$ shock conditions. It is important to recall that the method is biased towards clear signatures of $q_\perp$-like bow shock crossings, in practice filtering out many $q_\parallel$ crossings. About 22% of the $q_\perp$ crossings are highly perpendicular shocks ($\theta_{Bn} \geq 80°$, 2,674 crossings), whereas only $\sim$ 1% of the $q_\parallel$ shocks are highly parallel ones ($\theta_{Bn} \leq 10°$, 30 crossings). This is shown in Fig. 7, where the highest number of crossings occurs for $\theta_{Bn} \sim 80°$. This is also in qualitative agreement with the results of Vignes et al. (2002) for the MGS mission, when they investigated a proportion of 93 $q_\perp$ shocks for only 23 $q_\parallel$ shocks.

4 Results: application to the MAVEN datasets

In this section, 2D and 3D fits of the found bow shock locations with the MAVEN spacecraft for the November 2014–07 February 2021 period are presented. First, the detected shock locations are sorted by Martian year (MY32 to MY35 included), aerocentric solar longitude Ls range (four seasons centred on equinoxes and solstices), EUV flux (two regimes, one for higher solar flux and lower solar flux), and shock nature ($q_\perp$ or $q_\parallel$). These cases correspond to:

- Martian years 32 (incomplete), 33, 34 and 35, inspired by the work of Hall et al. (2019) on MEX datasets,
- Solar longitude Ls ranges from $[315° - 45°]$ (centred on Northern Hemisphere [NH] spring equinox), $[45°-135°]$ (NH summer solstice), $[135°-225°]$ (NH autumn equinox), $[225°-315°]$ (NH winter solstice). Ls defines the geographic Martian season, with Ls = 251° (Ls = 71°, respectively) marking perihelion (aphelion) conditions.
- Two EUV flux levels, inspired by the works of Halekas et al. (2017) and Gruesbeck et al. (2018) on the early MAVEN datasets. The EUV flux at Mars is obtained using the FISM-IUVS daily irradiances at 121.5 nm calculated from the Mars EUVM model (Thiemann et al., 2017). The median of the EUV flux in the 2014-2021 period is 0.0028 W/m^2 and defines two EUV flux levels, one "high" for fluxes above that limit, one "low" for fluxes below.

4.1 Statistical position of the Martian bow shock

2D case. In 2D MSO aberrated coordinates, the polar equation, Eq. (1), can be rewritten in the linear form $y = ax + b$ (see J. Trotignon et al., 2006):

$$r = L - \epsilon\,(X' - x_F)\,, \tag{23}$$

with a linear regression in the $(r, X' - x_F)$ space performed for a chosen focus location x_F. First a focus location is chosen randomly between 0 and $1\,R_{\rm p}$, and for each linear fit performed, the residuals are calculated. The adopted focus point is the one that minimises the residuals. Because MAVEN's orbits are not suited to bow shock detections for $X' < -0.5\,R_{\rm p}$, additional constraints on the tail distributions are necessary to obtain a more realistic conic fit. This can be achieved for example by using the predictions from a chosen pre-existing model for deeply negative X' values, such as those of Edberg et al. (2008) (noted 'E08' in the following) or Hall et al. (2019) (noted 'H19') where bow shock detections were reported downstream to $X'_{\rm min} \approx -1.5\,R_{\rm p}$ and to $\approx -5\,R_{\rm p}$, respectively. First, additional "ghost" points (representing 10% of the total number of detections for the considered case) are calculated for $X'_{\rm min} < X' < -0.5\,R_{\rm p}$ for the chosen model and randomised spatially around this result to give a more realistic tail spread. The linear regressions are then performed on the new constrained dataset. Tests were performed on the robustness of this method using different analytical models: E08 and H19 fits are essentially the same around the nose of the shock downstream to about $-1\,R_{\rm p}$ where patent differences start to appear. Because of the added cloud of ghost points, this is expected and thus 2D fits presented below are only valid in practice in the range $[-0.5\,R_{\rm p},\ R_{\rm ss}]$. Incidentally, differences on the terminator and subsolar standoff distances are less than $< 2\%$ in each case. It is noteworthy to add that the determination of the nature of the conic section found for the fits can be significantly altered when using tail models either from E08 (hyperbola) or from H19 (fits' nature given by these authors, ranging from ellipse to hyperbola, depend on the Martian year considered): in that case, the fit's nature will naturally be biased towards matching that of their respective parent tail model.

Table 3 and Fig. 8 display the 2D fits when the E08 tail model supplements the MAVEN dataset for additional constraints on the tail. Candidate bow shock detections are also drawn as semi-transparent circles. It is noteworthy to remark that, despite the constraints on the predictor-corrector algorithm, several detected points fall well into the magnetosheath of Mars, and are false detections. Because of their relative scarcity and thanks to the large statistical database, these points do not significantly impact the final fits, which remain robust.

Table 3. Martian bow shock 2D conic parameters in aberrated MSO coordinates from linear regression fits applied to Eq. (23) and the MAVEN orbits and magnetic field data (predictor-corrector algorithm). Subsolar and terminator standoff distances R_{ss} and R_{td} are calculated with Eqs. (5) and (6). For hyperbolae, the Mach cone aperture ϱ is also given as calculated by Eq. (7). For each fit, the coefficient of determination R^2 gives a measure of the goodness of the linear regression. Due to the large data spread, uncertainties on R_{ss} and R_{td} are of the order of 5% and of the order of 2% for the other quantities.

Case	ε	$L[R_p]$	$x_F[R_p]$	$R_{ss}[R_p]$	$R_{td}[R_p]$	R^2	Nature	$\varrho[^\circ]$	# detections
All points, this work	1.00	1.75	0.86	1.74	2.46	0.98	Parabola	–	14929
MY32, this work	0.83	2.24	0.65	1.87	2.70	0.97	Ellipse	–	1196
MY33, this work	0.99	1.88	0.75	1.69	2.51	0.98	Ellipse	–	4586
MY34, this work	1.02	1.72	0.84	1.69	2.44	0.96	Hyperbola	11	5073
MY35, this work	1.02	1.63	0.91	1.72	2.39	0.98	Hyperbola	11	4074
Ls = [315° − 45°], this work	1.01	1.73	0.86	1.72	2.45	0.98	Hyperbola	8	3793
Ls = [45° − 135°], this work	1.00	1.81	0.71	1.61	2.42	0.99	Parabola	–	3746
Ls = [135° − 225°], this work	0.99	1.82	0.71	1.62	2.42	0.98	Ellipse	–	3134
Ls = [225° − 315°], this work	0.98	1.91	0.86	1.82	2.62	0.98	Ellipse	–	4256
EUV flux ≥ 0.0028 W/m^2	1.00	1.79	0.91	1.80	2.54	0.98	Parabola	–	6502
EUV flux < 0.0028 W/m^2	1.00	1.75	0.79	1.67	2.41	0.98	Parabola	–	8427
Quasi-$\perp$	1.00	1.79	0.82	1.72	2.48	0.98	Parabola	–	11967
Quasi-$\parallel$	1.06	1.47	1.07	1.78	2.37	0.94	Hyperbola	19	2962

3D case. In 3D, a quadric fit is performed using the method first put forward by Taubin (1991), adapted to the quadratic surface of Eq. (9). This fitting method constructs scatter matrices from local gradients **S** of tested model **T** and finds the diagonal matrix of the generalised eigenvalue problem so that $\mathbf{Tv} = \lambda\mathbf{Sv}$, where **v** is the generalised eigenvector of **T** and **S**, and λ are the eigenvalues. Because of the scatter of points in the database, uncertainties on the found parameters A to I are of the order of 1%, in a least-squares sense.

Table 4 collects all 3D fit parameters for each case; all fitted surfaces are ellipsoids of revolution. The physical interpretation of these parameters in terms of principal axes, their direction and lengths and the centering of the ellipsoids is presented in Appendix Appendix A for completeness. Figure 9 shows the corresponding fits and their sections onto the X_{MSO} −

Table 4. Martian bow shock 3D conic parameters from quadric surface fits applied to the MAVEN orbits and magnetic field data (predictor-corrector algorithm). See Eq. (9) for the definition of parameters A to I and Eqs. (11), (12) and (13) for those of the subsolar standoff distance along the X_{MSO} axis and the terminator standoff distances along the Y_{MSO} and Z_{MSO} axes. Uncertainties on the parameters are of the order of 1% in a least squares sense. All quadrics below are ellipsoids. The domain of validity for each fit is shown in Fig. 9: fits are valid for $X_{\mathrm{MSO}} \geq -0.5\,R_p$ on average. The number of fitting points used for each case is the same as for the 2D fits, see Table 3 (last column). Also, see Appendix Appendix A for a physical interpretation of the tabulated parameters.

Case	A	B	C	D	E	F	G	H	I	R_{ss}	$R_{\mathrm{td,y}}$	$R_{\mathrm{td,z}}$
Gruesbeck et al. (2018)[a]	0.0490	0.1570	0.1530	0.0260	0.0120	0.0510	0.5660	-0.0310	0.0190	1.557	2.624	2.495
All points, this work	0.1769	0.1609	0.1559	0.0057	0.0044	0.0281	0.3773	-0.0323	0.0143	1.539	2.595	2.487
MY32, this work	0.1369	0.1419	0.1400	0.0381	0.0178	0.0547	0.3783	0.0044	0.0279	1.654	2.639	2.575
MY33, this work	0.1660	0.1516	0.1501	0.0235	-0.0061	0.0203	0.3807	-0.0284	-0.0018	1.562	2.664	2.587
MY34, this work	0.1719	0.1742	0.1551	-0.0112	-0.0068	0.0165	0.3955	-0.0256	0.0127	1.522	2.470	2.499
MY35, this work	0.5577	0.2245	0.2000	-0.0509	-0.0103	0.0963	-0.1421	0.0011	-0.0119	1.472	2.108	2.266
Ls = [315° − 45°], this work	0.1554	0.1625	0.1587	-0.0265	-0.0081	0.0023	0.4260	0.0013	0.0044	1.513	2.477	2.496
Ls = [45° − 135°], this work	0.1719	0.1761	0.1555	-0.0275	0.0048	0.0564	0.4107	-0.0287	0.0057	1.497	2.466	2.518
Ls = [135° − 225°], this work	0.2490	0.1473	0.2624	0.0409	0.0415	0.1098	0.2368	-0.0941	-0.1510	1.584	2.945	2.261
Ls = [225° − 315°], this work	0.1559	0.1484	0.1400	0.0047	0.0227	0.0400	0.3583	-0.0072	-0.0197	1.632	2.620	2.744
EUV flux ≥ 0.0028 W/m^2	0.1096	0.1480	0.1500	0.0274	0.0031	0.0355	0.4329	-0.0293	0.0045	1.634	2.700	2.567
EUV flux < 0.0028 W/m^2	0.2138	0.1807	0.1577	-0.0231	-0.0051	0.0314	0.3473	-0.0207	0.0185	1.498	2.410	2.460
Quasi-⊥	0.1798	0.1607	0.1539	0.0016	0.0040	0.0330	0.3777	-0.0348	0.0124	1.531	2.605	2.509
Quasi-∥	0.1427	0.1675	0.1666	-0.0004	0.0051	0.0050	0.3992	-0.0098	0.0230	1.595	2.473	2.382

[a]For *all points* considered in their data subset.

Y_{MSO} (dawn-dusk hemispheres), $X_{\mathrm{MSO}} - Z_{\mathrm{MSO}}$ (South-North hemispheres) and $Y_{\mathrm{MSO}} - Z_{\mathrm{MSO}}$ (at the terminator, i.e., $X_{\mathrm{MSO}} = 0$) non-aberrated MSO coordinates.

Because of the spacecraft changing orbits during the mission, some of the ellipsoid fits appear anomalous in their orientation. This is especially obvious for MY35 when MAVEN, as of Mars 2020, decreased its apogee to ∼ 4500 km and hence its revolution period to 3.5 h to accommodate Mars 2020 rover operations on the ground. Consequently, MAVEN only seldom explored regions below $X < 0\,R_p$ for half of MY35, which makes it difficult to constrain the fit, with ellipsoid having its longest principal axis tilted almost 90° in the X-Z plane (panel A, purple curves of Fig. 9). A similar issue is found for Ls = 135–225° (panel B, yellow, Fig. 9), which has the lowest number of detections among Ls ranges and for which the orbit was never favourable for detections due to orbit precession. Thus, in these two cases, no physical interpretation should be drawn from the axes orientations of the ellipsoid and the fit should be only valid for near-subsolar crossings. More robust physics-based analytical models could be used to overcome these fitting issues (Kotova et al., 2021).

654 ### 4.2 Discussion

655 The 2D and 3D fits performed above give some insight on how the Martian bow shock
656 is moving globally for different conditions of Martian Year, Ls and EUV flux and complements
657 previous studies with the MAVEN mission (Halekas et al., 2017; Gruesbeck et al., 2018). As
658 the bow shock position is connected to the balance between thermal pressure from the plasma
659 in the ionosphere and the dynamical pressure from the solar wind, any variation of these two
660 quantities will have repercussions on the position of the shock.

661 When assuming axisymmetry around the aberrated axis X' in the 2D polar rectangular
662 coordinates case, Table 2 and the average subsolar and terminator distances can be a first guide
663 for interpretation. Our new results with MAVEN (all points, Table 3) agree rather well with
664 past measurements (Table 2) considering the data spread and estimated uncertainties: $R_{ss} =$
665 1.74 ± 0.09 compared to $1.61 \pm 0.08\,R_p$ and $R_{td} = 2.46 \pm 0.13$ compared to $2.56 \pm 0.20\,R_p$.
666 More specifically, for:

667 - Martian Years: the subsolar standoff distance decreases by as much as 10% between
668 MY32 and MY33–MY34, from 1.87 to $1.69\,R_p$, although some of this variation may
669 be stemming from the relatively lower statistics for the first year (1,196 points for MY32
670 compared to $> 4,000$ for all other years), due to the MAVEN mission starting towards
671 the end of MY32. A similar tendency is seen for terminator standoff distances, with a
672 11% decrease seen between MY32 and MY35. Following Hall et al. (2019), these vari-
673 ations may be connected through solar EUV irradiance to the solar cycle itself, when
674 descending from the maximum of solar cycle 24 (encompassed by MY32) towards a
675 minimum of activity (MY34) and the start of solar cycle 25 (MY35). A variation in R_{ss}
676 of similar magnitude ($\sim 7\%$ between minimum and maximum of activity) was shown
677 by Hall et al. (2019) using MEX data for the previous solar cycles (23–24).
678 - Seasonal variations: in contrast, the Ls ranges have a much more even statistics through-
679 out, with more than 3,000 detections per season. Arguably, this makes comparing re-
680 sults between seasons statistically more significant than for the previous case. Overall,
681 for northern spring equinox (Ls = [315°−45°]) and winter solstice (Ls = [225°−315°])
682 conditions, the bow shock appears to expand in the subsolar direction by about 7−13%
683 from its summer and autumn position ($R_{ss} \geq 1.72\,R_p$ compared to $R_{ss} \approx 1.61\,R_p$). Si-
684 multaneously, the area encompassed by the bow shock conic is also increased during
685 those two instances. One possible driving factor behind these changes may be in turn

linked to changes in Mars' dayside upper atmosphere and extended exosphere, and how they expand and contract with seasons, increasing or decreasing the size of the obstacle to the solar wind flow (Hall et al., 2016, and references therein). A denser lower atmosphere around perihelion (Ls ~ 251° where the EUV flux is highest on average) and during the dust storm season in the autumn (Trainer et al., 2019) may drive the ionosphere to expand significantly at constant EUV flux (Sánchez-Cano et al., 2016; Dubinin et al., 2019), offering a more efficient obstacle to the solar wind. Similarly the expansion of Mars' extended exosphere (notably modulated by the solar wind flux) increases the efficiency of the solar wind charge exchange process (with a net conversion of fast solar wind ions to slow-moving heavy ions of planetary origin, effectively slowing down the solar wind, see Edberg et al., 2009; Halekas et al., 2017). Both aspects result in the standoff distance moving outwards. The opposite effect is expected when upper atmosphere densities are lower in the deep summer and in the beginning of the autumn and the bow shock surface shrinks. The fits and characteristics of the shock appear consistent with this picture.

- EUV flux variations: the effect of a relatively larger flux on the shock position is twofold, globally increasing the ionisation rates in the ionosphere and through photoionisation of the extended exosphere as well as heating up and expanding the neutral atmosphere-exosphere system (Forbes et al., 2008; Edberg et al., 2009; Hall et al., 2016). Photoionisation of exospheric neutrals creates newly born ions that are picked up by the solar wind convective electric field, resulting in mass-loading and slowing down of the solar wind flow (Yamauchi et al., 2015, with the presence of pickup ions in the foreshock region). Such combined effects have been shown to expand the bow shock in the solar wind direction (Mazelle et al., 2004). The two fits presented here, one for higher and one for lower EUV fluxes (more than 6500 points each), display the expected behaviour, with a larger standoff distance by 7% and a noticeably larger flaring of the fitted conic for the higher EUV fluxes (terminator distances increasing from 2.41 to 2.54 R_p , i.e., 5%).
- Shock conditions: $q_{\parallel}$ and $q_{\perp}$ bow shock crossings are related to the average interplanetary magnetic field's (IMF) direction and the spacecraft's orbit (more precisely, the spherical quadrant in which the spacecraft emerges into the solar wind). Because the predictor-corrector algorithm favours $q_{\perp}$ detections (Sect. 3.2), the statistics between the two cases is heavily unbalanced (see Vignes et al., 2002, for a similar result). On average, no sig-

nificant difference between the two conditions can be seen, with the shock surface slightly contracting and flaring up in $q_\perp$ conditions with respect to $q_\parallel$ conditions ($|\Delta R_{ss,td}| \sim 4\%$). Such a tendency is marginal considering that these percentages are at the precision limit obtained with the fits.

Let us now look at the 3D fit results. Figure 9 clearly shows several asymmetries depending on the Martian year, Ls, EUV flux and shock condition. The usual North-South asymmetry ($X_{MSO} - Z_{MSO}$ plane, second column, and also $Y_{MSO} - Z_{MSO}$ plane, third column) due to the presence of crustal magnetic fields in the southern hemisphere is clearly seen for all cases with the standoff subsolar distances being skewed towards that hemisphere. This is shown by crosses representing the tip of the projected ellipsoid (calculated by the formulae in Appendix Appendix B) located all in the fourth quadrant in the $X_{MSO}-Z_{MSO}$ plane. A similar tendency is sometimes marginally observed in the $X_{MSO}-Y_{MSO}$ plane (first column), when the shock surface is skewed towards the dawn hemisphere ($-Y_{MSO}$), with standoff subsolar distances on average larger than on the dusk hemisphere. This is true for MY32 and MY33 (panel A) and for larger EUV fluxes (panel C). For lower EUV fluxes (and, incidentally, all other cases), the opposite seems to be taking place with the position of the maximum standoff distance being in the dusk $+Y_{MSO}$ hemisphere. It is difficult at this stage to tell if these latter (small) effects may stem mainly or not from the dawn-dusk asymmetry of the atmosphere and hence of the ionosphere Gupta et al. (2019).

Comparison between all standoff distances, subsolar and terminator alike, and calculated by the 2D and 3D algorithms is shown in Fig. 10 and based on Tables 3 and 4. The standoff distances calculated from the 3D fits show the same tendencies as their 2D counterparts, although since the X and Y coordinates are not solar-wind aberrated and hence no axisymmetry is considered, the comparison between the 2D and 3D cases can only be that of general trends. From MY32 to MY35, a general decrease of standoff distances can be seen. Excluding R_{tdy}, the other standoff distances first steadily decrease from Ls centred on 0° (labelled "Ls1") to 180° ("Ls3") but then increase significantly towards Ls values around 270° ("Ls4"), which may be linked to the EUV flux becoming maximum at perihelion Ls = 251°. This result is arguably in contrast to those presented in Vignes et al. (2002) although our statistics with MAVEN is much larger than in their study. In an identical way to the 2D fits, larger EUV fluxes result in a bow shock surface significantly expanding in the solar wind towards the subsolar direction. With respect to the nature of the shock, the subsolar standoff distances R_{ss} appear to

marginally increase from $q_\perp$ to $q_\parallel$ conditions, although the inverse trend is seen for the terminator distances. Again, these differences are slight, which may reflect in part the bias against $q_\parallel$ conditions of our bow shock estimator (thus yielding a low amount of $q_\parallel$ shock detections).

As a preliminary conclusion, it is important to note that:

- The $X_{\mathrm{MSO}} - Y_{\mathrm{MSO}}$ and $X_{\mathrm{MSO}} - Z_{\mathrm{MSO}}$ asymmetry seems particularly marked for Ls = [135° − 225°] (labelled "Ls3" on the figure), MY32, MY35 and higher EUV fluxes: it can readily be seen by comparing the length of the blue and red bars. As explained earlier, the number of points used for fits for MY32 is the lowest of all the cases because MAVEN arrived at Mars late in MY32. This is in qualitative agreement with the conclusions of Gruesbeck et al. (2018). On average and outside of those special cases, the shock's shape stays rather symmetric about the X_{MSO} axis: the terminator distances R_{td_z} (3D fits) and R_{td} (2D fits) indeed seem to match rather well most of the time. This axisymmetric tendency can be further amplified by aligning the $X_{\mathrm{MSO}} - Y_{\mathrm{MSO}}$ plane with the solar wind aberration system, rotating the 3D quadric surface 4 degrees anticlockwise around the Z_{MSO} axis; new standoff distances for the 3D fits (R_{td_z} and R_{ss}) differ by less than 5% with their corresponding 2D fits values (not shown).
- Although the 3D and 2D conic fits retain strong similarities in their behaviour, the 3D fits (seemingly paradoxically) appear more robust and less affected by external assumptions. It is recalled here that not only do the 2D fits assume axisymmetry around X'_{MSO}, but certain 2D fits had to also be constrained at larger euclidean distances from the centre of the planet due to the poor coverage of MAVEN for $X'_{\mathrm{MSO}} < 0.5\,R_{\mathrm{p}}$. This superiority of the 3D fitting algorithm is due to: (i) the number of fitting variables (A to I, allowing more flexibility despite risking over-determination of the linear system of equations), (ii) the natural asymmetry of the shock (albeit small), and (iii) the fitting points being statistically better distributed over a larger space (both in X_{MSO}−Y_{MSO} and X_{MSO}−Z_{MSO} planes instead of a single polar plane) and thus optimising the fits.
- Because the Martian seasons (monitored by Ls ranges) to a degree and the EUV flux both depend on Mars' heliocentric distance, correlations between these fits are to be expected. For example, similar fits for low Ls values (< 135°) and low EUV flux can be seen in Figs. 8 (panels C and E, orange curves) and 9 (panels B and C, red curves).
- Because the solar cycle is a continuous underlying driver of the shock's position regardless of the binnings adopted here, correlations between EUV flux and Mars year results

783 are also expected. This effect is most clearly exemplified with the shock standoff de-
784 crease when going from the declining phase of solar cycle 24 (MY32 and MY33, high
785 fluxes) to the next solar minimum (MY34, low fluxes).

786 5 Conclusions

787 In this study, we presented a "fast and dirty" method to estimate automatically the lo-
788 cation of the bow shock in real spacecraft orbits, as well as analytical expressions for the nor-
789 mal direction to the shock surface at any point in its close vicinity. After a survey of exist-
790 ing analytical smooth models of the bow shock surface at the planet Mars based on 2D and
791 3D fits, we used these models as a first prediction of the shock location in the data and re-
792 fined this prediction further with a predictor-corrector algorithm based on the median abso-
793 lute deviation of the magnetic field around the predicted shock. This method, biased towards
794 the detection of $q_\perp$ shocks but not entirely limited to them, does not substitute for a detailed
795 analysis of the crossing or for machine-learning techniques currently developed for space mis-
796 sions. It however finds a useful application when it is necessary to quickly determine the po-
797 sition of the spacecraft, or at least an estimate thereof, with respect to the bow shock.

798 As part of the solar wind and space weather database Helio4Cast (Möstl et al., 2020),
799 the technique was successfully used to retrieve solar wind undisturbed parameters from the
800 MAVEN mission. We also successfully applied the predictor-corrector method to the MAVEN
801 orbit and magnetic field data between November 2014 and February 2021, and performed a
802 series of fits, in 2D and in 3D, to investigate statistically the shape of the shock depending on
803 Martian Year, solar longitude Ls, and two solar EUV flux levels. The 3D fitting has obvious
804 advantages over the 2D polar axisymmetric geometry usually used to describe the shock struc-
805 ture, namely, a more accurate estimate of asymmetries in the global structure, and taking full
806 advantage of the 3D distribution of bow shock detections in space. This is especially impor-
807 tant for bodies with large orbital eccentricities and axial tilts to the ecliptic such as Mars, for
808 which the heliocentric distance is a strong driver of the EUV flux input and seasonal changes
809 on the planet. Expectedly, the Martian shock was found to be highly asymmetric with respect
810 to the North-South hemispheres due to the presence of crustal magnetic field anomalies, in agree-
811 ment with previous studies (see for example Hall et al., 2016; Halekas et al., 2017; Gruesbeck
812 et al., 2018). Bow shock fits for quasi-perpendicular and parallel shock conditions were, to
813 the precision of our approach, almost identical. In addition, the shock appeared noticeably asym-
814 metric with respect to Y_{MSO} and Z_{MSO} directions in specific conditions, namely, for MY32 and

MY35, Ls = [135°−225°] and larger EUV fluxes. Despite this, the solar aberrated axisymmetric system provides a worthy first approximation of the shock's shape and position.

To investigate further the conditions of the shock's asymmetry throughout different solar cycles, a reanalysis of past encounters at Mars using 3D quadric fits would be a welcome addition. Applications of these methods, especially in 3D, to other bodies with large orbital eccentricities (such as Mercury) will also prove of interest.

Appendix A Characteristics of a quadric surface

The 3D planetary bow shock in this paper is approximated as a quadratic surface described by the Cartesian equation (9). Mathematically, 17 different quadrics can exist. However, here only 3 are physically acceptable for the approximation of a bow shock surface. These are the *'real' ellipsoid*, the *elliptic paraboloid*, and the *hyperboloid of two sheets*. From coefficients A to I defining the quadric's surface equation, it is possible to extract some more 'physical' quantities of these surfaces such as the centre of the surface, the direction of the principal axes, the typical length, or the 'nose' of the surface. This requires the analysis of one particular matrix $\mathbf{M}$ given by:

$$\mathbf{M} = \begin{pmatrix} A & D/2 & F/2 \\ D/2 & B & E/2 \\ F/2 & E/2 & C \end{pmatrix}. \tag{A1}$$

Determinant $\det \mathbf{M}$ yields useful pieces of information on the considered surface. If $\det \mathbf{M} < 0$, the surface is an ellipsoid or an hyperboloid of two sheets. If $\det \mathbf{M} = 0$, it is an elliptic paraboloid.

The coordinates of the centre of the surface is given by:

$$\mathbf{P}_{\text{centre}} = -\mathbf{M}^{-1} \begin{pmatrix} G/2 \\ H/2 \\ I/2 \end{pmatrix}$$

if $\mathbf{M}^{-1}$ exists. In the case of an elliptic paraboloid, there is an infinite number of centres placed along the intersections of the two planes of symmetry.

836 As **M** is symmetric, its eigenvalues are real and eigenvectors are orthogonal. Let us de-
837 fine λ_i ($i = 1, 2, 3$), the eigenvalues of **M**, and $\mathcal{V}_i$, their associated eigenvectors. Physically,
838 only 3 cases should be considered:

839 • ellipsoid: $\lambda_1, \lambda_2, \lambda_3 > 0$. $1/\sqrt{\lambda_i}$ are proportional with the same constant to the length
840 of the conic along the three principal axes of the ellipsoid,
841 • elliptic paraboloid: $\lambda_1, \lambda_2 > 0$ and $\lambda_3 = 0$,
842 • hyperboloid of two sheets: $\lambda_1, \lambda_2 < 0$ and $\lambda_3 > 0$. The characteristic lengths of the
843 hyperboloid are proportional to $1/\sqrt{|\lambda_i|}$.

844 Finally, one may be interested in the position of the tip (tail-like direction) or of the nose
845 (subsolar direction) of the surface. These extremum points are at a distance L_1, L_2, and L_3 from
846 the centre in the direction $\pm\mathcal{V}_i$. Therefore they are given by:

$$L_i = \sqrt{\lambda_i}\,\sqrt{\mathbf{P}_{\text{centre}}^T\,\mathbf{M}\,\mathbf{P}_{\text{centre}} + 1}$$

847 and

$$\mathbf{P}_{\pm,\text{ext}} = \mathbf{P}_{\text{centre}}\begin{pmatrix}1 & 1 & 1\end{pmatrix} \pm \begin{pmatrix}L_1\mathcal{V}_1 & L_2\mathcal{V}_2 & L_3\mathcal{V}_3\end{pmatrix} \tag{A2}$$

848 where the columns of $\mathbf{P}_{\pm,\text{ext}}$ are the locations of the extrema. For a hyperboloid of two sheets,
849 only the real solution associated with λ_3 should be considered: this gives the position of the
850 noses or tips of both sheets. The sunward-most position of the ellipsoid (its nose) is referred
851 to as $\mathbf{P}_{\text{nose}}$.

852 The tip or nose of the ellipsoid is in our context along the direction of the eigenvectors
853 with the largest X (in absolute value) component.

854 The volume of the ellipsoid is:

$$\mathrm{V} = \frac{4}{3}\pi\, L_1\, L_2\, L_3. \tag{A3}$$

855 Table A1 presents the length of each of the three principal axes of the quadric L_i, the
856 ellipsoid's volume, eigenvectors $\mathcal{V}_i$ and the coordinates of the centre and sunward nose of the
857 surface for each ellipsoid in Table 4.

858 Appendix B Subsolar tip of the trace of an ellipsoid surface in Cartesian coordinates

859 The subsolar point of the projection of a 3D ellipsoid in 2D planes, as shown in Fig. 9
860 (crosses), can be obtained by finding the roots of the corresponding 2D conic in the plane con-

Table A1. Characteristics of the 3D Martian bow shock as derived from the MAVEN dataset, see Table 4 for the parameters of the 3D surfaces considered. All quadrics are ellipsoids. L_i ($i = 1, 2, 3$) are the lengths in units of R_p of the principal axes of the ellipsoids and V their volume. $\mathcal{V}_i$ are the eigenvectors of matrix $\mathbf{M}$, i.e., the normalised directions of the principal axes in MSO Cartesian coordinates. $\mathbf{P}_{\text{centre}}$ and $\mathbf{P}_{\text{nose}}$ are the positions of the centre of the ellipsoid and its sunward nose, in MSO Cartesian coordinates. The domain of validity for each fit is shown in Fig. 9: fits are valid for $X_{\text{MSO}} \geq -0.5\,R_p$ on average.

Case	L_1	L_2	L_3	Volume V	$\mathcal{V}_1$			$\mathcal{V}_2$			$\mathcal{V}_3$			$\mathbf{P}_{\text{centre}}$ $[R_p]$			$\mathbf{P}_{\text{nose}}$ $[R_p]$		
		$[R_p]$		$[R_p^3]$	X_{MSO}	Y_{MSO}	Z_{MSO}	X_{MSO}	Y_{MSO}	Z_{MSO}	X_{MSO}	Y_{MSO}	Z_{MSO}	X_{MSO}	Y_{MSO}	Z_{MSO}	X_{MSO}	Y_{MSO}	Z_{MSO}
Gruesbeck+ (2018), all points	8.20	4.34	4.11	613.30	-0.97	0.10	0.22	0.08	-0.72	0.69	0.22	0.69	0.69	-6.45	0.59	0.99	1.52	-0.21	-0.80
All points, this work	2.84	2.74	2.55	83.37	-0.44	-0.06	0.90	-0.16	0.99	-0.01	-0.88	-0.15	-0.45	-1.07	0.12	0.05	1.18	0.50	1.19
MY32, this work	3.42	3.09	2.68	118.38	0.76	-0.28	-0.59	0.13	-0.82	0.55	0.64	0.50	0.59	-1.44	0.17	0.17	1.16	-0.79	-1.83
MY33, this work	2.97	2.82	2.65	92.83	-0.50	0.61	0.62	-0.06	0.69	-0.72	-0.87	-0.40	-0.31	-1.17	0.19	0.09	1.13	1.23	0.90
MY34, this work	2.85	2.70	2.60	83.79	-0.37	0.05	0.93	-0.65	-0.73	-0.21	0.67	-0.68	0.30	-1.15	0.04	0.02	0.60	-1.73	0.80
MY35, this work	2.28	2.13	1.34	27.19	-0.13	0.06	0.99	0.08	1.00	-0.05	-0.99	0.08	-0.13	0.13	0.01	-0.00	1.45	-0.09	0.17
Ls = [315° − 45°], this work	2.99	2.86	2.73	97.79	0.78	0.62	0.12	-0.25	0.13	0.96	0.58	-0.78	0.25	-1.38	-0.12	-0.01	0.94	1.73	0.34
Ls = [45° − 135°], this work	3.08	2.68	2.52	87.10	-0.61	-0.23	0.76	0.21	0.87	0.44	-0.76	0.43	-0.48	-1.23	-0.02	0.20	0.69	-1.10	1.42
Ls = [135° − 225°], this work	2.80	2.36	1.88	51.95	0.13	-0.99	0.11	0.74	0.03	-0.67	0.65	0.17	0.74	-0.59	0.35	0.38	1.17	0.41	-1.19
Ls = [225° − 315°], this work	3.13	2.86	2.65	99.65	-0.48	-0.33	0.81	-0.47	0.88	0.08	-0.74	-0.34	-0.58	-1.18	0.02	0.24	0.79	0.94	1.76
EUV flux ≥ 0.0028 W/m^2	3.81	3.13	3.00	150.08	-0.92	0.25	0.32	-0.02	-0.81	0.58	-0.40	-0.53	-0.75	-2.05	0.29	0.22	1.44	-0.67	-0.98
EUV flux < 0.0028 W/m^2	2.73	2.54	2.27	65.77	-0.26	-0.02	0.97	-0.27	-0.96	-0.09	0.93	-0.28	0.24	-0.81	0.01	0.02	1.30	-0.63	0.57
Quasi-$\perp$	2.87	2.73	2.53	83.11	-0.43	-0.10	0.90	-0.09	0.99	0.06	-0.90	-0.06	-0.44	-1.06	0.11	0.07	1.21	0.26	1.18
Quasi-$\parallel$	3.00	2.79	2.75	96.12	-0.99	-0.02	0.10	0.09	-0.66	0.75	0.06	0.75	0.66	-1.40	0.03	-0.05	1.58	0.08	-0.36

manuscript submitted to *JGR: Space Physics*

sidered. For $z = 0$, Eq. (9) becomes a second order equation:

$$Ax^2 + By^2 + Dxy + Gx + Hy - 1 = 0. \tag{B1}$$

Fixing variable y, the equation can be put in quadratic form with the following positive root:

$$x_{\mathrm{M}} = \frac{-(Dy + G) + \sqrt{\Delta}}{2A}, \tag{B2}$$

$$\Delta = (Dy + G)^2 - 4A\left(By^2 + Hy - 1\right) > 0 \tag{B3}$$

Finding the maximum of this function is equivalent to finding a y value that maximises this function. Posing $\xi = Dy + G$, its derivative has the form:

$$\frac{\partial x_{\mathrm{M}}}{\partial y} = \frac{2D\xi - 4A(2By + H)}{4A\sqrt{\xi^2 - 4A\left(By^2 + Hy - 1\right)}} - \frac{D}{2A} \tag{B4}$$

Solving $\frac{\partial x_{\mathrm{M}}}{\partial y} = 0$ for y and using that result in Eq. (B2) makes it possible to calculate the final (x, y) coordinates of the projected ellipsoid's tip in the corresponding x–y plane. An identical reasoning can be made for the $x - z$ plane.

This tip in a plane is however not necessarily the farthest subsolar point of the ellipsoid's surface. Its position in 3D is by contrast given by Eq. (A2) in Appendix Appendix A.

Acknowledgments

C. Simon Wedlund, M. Volwerk and C. Möstl thank the Austrian Science Fund (FWF): P32035-N36, P31659-N27, P31521-N27. A. Beth thanks the Swedish National Space Agency (SNSA) and its support with the grant 108/18. Parts of this work for the observations obtained with the SWEA instrument are supported by the French space agency CNES.The FISM-P Mars Solar Spectral Irradiance model is for instance available at `https://lasp.colorado.edu/lisird/data/fism_p_ssi_mars/`. The authors acknowledge Emmanuel Penou for help and access to the CLWeb software (v16.09) from IRAP/Observatoire Midi-Pyrénées. The Helio4Cast database is available at `www.helioforecast.space/icmecat` and `www.helioforecast.space/sircat`. The authors thank Dr. Jared Espley (NASA) for his support in using MAVEN/MAG data. The calibrated MAVEN/MAG datasets are available from the NASA Planetary Data System (PDS). CSW acknowledges L. Hunyadi for the matrix implementation of the Taubin 3D fitting algorithm, and Yair Altman for developing and maintaining the Matlab package "export_fig" for figure pdf exports. The authors would like to acknowledge ISSI for the opportunity it offered for very valuable discussions on this topic as part of the International Team #499 "Similarities and Differences in the Plasma at Comets and Mars" led by C. Götz during these hard Covid times.

References

Balogh, A., & Treumann, R. A. (2013). *Physics of Collisionless Shocks: Space Plasma Shock Waves*. New York: Springer-Verlag. Retrieved 2020-08-11, from https://www.springer.com/gp/book/9781461460985 doi: 10.1007/978-1-4614-6099-2

Barabash, S., Lundin, R., Andersson, H., Brinkfeldt, K., Grigoriev, A., Gunell, H., ... Thocaven, J.-J. (2006, October). The Analyzer of Space Plasmas and Energetic Atoms (ASPERA-3) for the Mars Express Mission. *Space Sci Rev*, *126*(1), 113–164. Retrieved 2021-03-18, from https://doi.org/10.1007/s11214-006-9124-8 doi: 10.1007/s11214-006-9124-8

Biermann, L. (1951). Kometenschweife und solare Korpuskularstrahlung. *Zeitschrift fur Astrophysik*, *29*, 274. Retrieved 2020-08-03, from http://adsabs.harvard.edu/abs/1951ZA.....29..274B

Burgess, D., Lucek, E. A., Scholer, M., Bale, S. D., Balikhin, M. A., Balogh, A., ... Walker, S. N. (2005). Quasi-parallel Shock Structure and Processes. In G. Paschmann, S. J. Schwartz, C. P. Escoubet, & S. Haaland (Eds.), *Outer Magnetospheric Boundaries: Cluster Results* (Vol. 20, pp. 205–222). Dordrecht: Springer Netherlands. Retrieved 2020-08-11, from https://doi.org/10.1007/1-4020-4582-4_7 doi: 10.1007/1-4020-4582-4_7

Burgess, D., & Scholer, M. (2014). Microphysics of Quasi-parallel Shocks in Collisionless Plasmas. In A. Balogh, A. Bykov, P. Cargill, R. Dendy, T. Dudok de Wit, & J. Raymond (Eds.), *Microphysics of Cosmic Plasmas* (pp. 437–457). Boston, MA: Springer US. Retrieved 2021-03-18, from https://doi.org/10.1007/978-1-4899-7413-6_17 doi: 10.1007/978-1-4899-7413-6_17

Connerney, J. E. P., Espley, J., Lawton, P., Murphy, S., Odom, J., Oliversen, R., & Sheppard, D. (2015, December). The MAVEN Magnetic Field Investigation. *Space Sci Rev*, *195*(1-4), 257–291. Retrieved 2019-10-10, from http://link.springer.com/10.1007/s11214-015-0169-4 doi: 10.1007/s11214-015-0169-4

Dubinin, E., Fraenz, M., Pätzold, M., Woch, J., McFadden, J., Halekas, J. S., ... Zelenyi, L. (2019). Expansion and Shrinking of the Martian Topside Ionosphere. *Journal of Geophysical Research: Space Physics*, *124*(11), 9725–9738. Retrieved 2021-03-18, from http://agupubs.onlinelibrary.wiley.com/doi/abs/10.1029/2019JA027077 (_eprint: https://onlinelibrary.wiley.com/doi/pdf/10.1029/2019JA027077) doi: https://doi.org/

10.1029/2019JA027077

Dubinin, E., Fränz, M., Woch, J., Roussos, E., Barabash, S., Lundin, R., ... Acuña, M. (2006, October). Plasma Morphology at Mars. Aspera-3 Observations. *Space Sci Rev*, *126*(1), 209–238. Retrieved 2020-08-03, from https://doi.org/10.1007/s11214-006-9039-4 doi: 10.1007/s11214-006-9039-4

Edberg, N. J. T., Brain, D. A., Lester, M., Cowley, S. W. H., Modolo, R., Fränz, M., & Barabash, S. (2009, September). Plasma boundary variability at Mars as observed by Mars Global Surveyor and Mars Express. *Annales Geophysicae*, *27*(9), 3537–3550. Retrieved 2020-08-03, from https://angeo.copernicus.org/articles/27/3537/2009/angeo-27-3537-2009.html (Publisher: Copernicus GmbH) doi: https://doi.org/10.5194/angeo-27-3537-2009

Edberg, N. J. T., Lester, M., Cowley, S. W. H., Brain, D. A., Fränz, M., & Barabash, S. (2010). Magnetosonic Mach number effect of the position of the bow shock at Mars in comparison to Venus. *Journal of Geophysical Research: Space Physics*, *115*(A7). Retrieved 2020-08-03, from http://agupubs.onlinelibrary.wiley.com/doi/abs/10.1029/2009JA014998 (_eprint: https://onlinelibrary.wiley.com/doi/pdf/10.1029/2009JA014998) doi: 10.1029/2009JA014998

Edberg, N. J. T., Lester, M., Cowley, S. W. H., & Eriksson, A. I. (2008, August). Statistical analysis of the location of the Martian magnetic pileup boundary and bow shock and the influence of crustal magnetic fields: STATISTICAL ANALYSIS OF MPB AND BS. *J. Geophys. Res.*, *113*(A8), n/a–n/a. Retrieved 2019-09-20, from http://doi.wiley.com/10.1029/2008JA013096 doi: 10.1029/2008JA013096

Forbes, J. M., Lemoine, F. G., Bruinsma, S. L., Smith, M. D., & Zhang, X. (2008). Solar flux variability of Mars' exosphere densities and temperatures. *Geophysical Research Letters*, *35*(1). Retrieved 2019-11-20, from http://agupubs.onlinelibrary.wiley.com/doi/abs/10.1029/2007GL031904 doi: 10.1029/2007GL031904

Formisano, V. (1979, September). Orientation and shape of the Earth's bow shock in three dimensions. *Planetary and Space Science*, *27*(9), 1151–1161. Retrieved 2019-10-15, from http://www.sciencedirect.com/science/article/pii/0032063379901351 doi: 10.1016/0032-0633(79)90135-1

Formisano, V., Domingo, V., & Wenzel, K. P. (1979, September). The three-dimensional shape of the magnetopause. *Planetary and Space Science*, *27*(9), 1137–1149. Re-

trieved 2019-10-15, from http://www.sciencedirect.com/science/article/pii/003206337990134X doi: 10.1016/0032-0633(79)90134-X

Gary, S. P. (1992). The mirror and ion cyclotron anisotropy instabilities. *J. Geophys. Res.*, *97*(A6), 8519. Retrieved 2019-09-16, from http://doi.wiley.com/10.1029/92JA00299 doi: 10.1029/92JA00299

Gringauz, K. I., Bezrukikh, V. V., Verigin, M. I., & Remizov, A. P. (1976). On electron and ion components of plasma in the antisolar part of near-Martian space. *Journal of Geophysical Research (1896-1977)*, *81*(19), 3349–3352. Retrieved 2020-02-05, from http://agupubs.onlinelibrary.wiley.com/doi/abs/10.1029/JA081i019p03349 doi: 10.1029/JA081i019p03349

Gruesbeck, J. R., Espley, J. R., Connerney, J. E. P., DiBraccio, G. A., Soobiah, Y. I., Brain, D., ... Mitchell, D. L. (2018). The Three-Dimensional Bow Shock of Mars as Observed by MAVEN. *Journal of Geophysical Research: Space Physics*, *123*(6), 4542–4555. Retrieved 2019-10-14, from https://agupubs.onlinelibrary.wiley.com/doi/abs/10.1029/2018JA025366 doi: 10.1029/2018JA025366

Gupta, N., Venkateswara Rao, N., & Kadhane, U. R. (2019, December). Dawn-Dusk Asymmetries in the Martian Upper Atmosphere. *Journal of Geophysical Research (Planets)*, *124*(12), 3219-3230. doi: 10.1029/2019JE006151

Halekas, J. S., Ruhunusiri, S., Harada, Y., Collinson, G., Mitchell, D. L., Mazelle, C., ... Jakosky, B. M. (2017). Structure, dynamics, and seasonal variability of the Mars-solar wind interaction: MAVEN Solar Wind Ion Analyzer in-flight performance and science results. *Journal of Geophysical Research: Space Physics*, *122*(1), 547–578. Retrieved 2019-10-29, from https://agupubs.onlinelibrary.wiley.com/doi/abs/10.1002/2016JA023167 doi: 10.1002/2016JA023167

Halekas, J. S., Taylor, E. R., Dalton, G., Johnson, G., Curtis, D. W., McFadden, J. P., ... Jakosky, B. M. (2015, December). The Solar Wind Ion Analyzer for MAVEN. *Space Sci Rev*, *195*(1), 125–151. Retrieved 2019-10-29, from https://doi.org/10.1007/s11214-013-0029-z doi: 10.1007/s11214-013-0029-z

Hall, B. E. S., Lester, M., Sánchez-Cano, B., Nichols, J. D., Andrews, D. J., Edberg, N. J. T., ... Orosei, R. (2016). Annual variations in the Martian bow shock location as observed by the Mars Express mission. *Journal of Geophysical Research: Space Physics*, *121*(11), 11,474–11,494. Retrieved 2019-10-14, from https://agupubs.onlinelibrary.wiley.com/doi/abs/10.1002/2016JA023316 doi:

10.1002/2016JA023316

Hall, B. E. S., Sánchez-Cano, B., Wild, J. A., Lester, M., & Holmström, M. (2019). The Martian Bow Shock Over Solar Cycle 23–24 as Observed by the Mars Express Mission. *Journal of Geophysical Research: Space Physics*, *124*(6), 4761–4772. Retrieved 2019-10-14, from https://agupubs.onlinelibrary.wiley.com/doi/abs/10.1029/2018JA026404 doi: 10.1029/2018JA026404

Horbury, T. S., Cargill, P. J., Lucek, E. A., Eastwood, J., Balogh, A., Dunlop, M. W., … Georgescu, E. (2002). Four spacecraft measurements of the quasiperpendicular terrestrial bow shock: Orientation and motion. *Journal of Geophysical Research: Space Physics*, *107*(A8), SSH 10–1–SSH 10–11. Retrieved 2021-03-18, from http://agupubs.onlinelibrary.wiley.com/doi/abs/10.1029/2001JA000273 (_eprint: https://onlinelibrary.wiley.com/doi/pdf/10.1029/2001JA000273) doi: https://doi.org/10.1029/2001JA000273

Kennel, C. F., Edmiston, J. P., & Hada, T. (1985). A Quarter Century of Collisionless Shock Research. In *Collisionless Shocks in the Heliosphere: A Tutorial Review* (pp. 1–36). American Geophysical Union (AGU). Retrieved 2019-11-05, from http://agupubs.onlinelibrary.wiley.com/doi/abs/10.1029/GM034p0001 doi: 10.1029/GM034p0001

Kotova, G., Verigin, M., Gombosi, T., Kabin, K., Slavin, J., & Bezrukikh, V. (2021). Physics-Based Analytical Model of the Planetary Bow Shock Position and Shape. *Journal of Geophysical Research: Space Physics*, *126*(6), e2021JA029104. Retrieved 2021-05-27, from http://agupubs.onlinelibrary.wiley.com/doi/abs/10.1029/2021JA029104 (_eprint: https://onlinelibrary.wiley.com/doi/pdf/10.1029/2021JA029104) doi: https://doi.org/10.1029/2021JA029104

Liu, D., Rong, Z., Gao, J., He, J., Klinger, L., Dunlop, M. W., … Wei, Y. (2021, April). Statistical Properties of Solar Wind Upstream of Mars: MAVEN Observations. *Astrophys. J.*, *911*(2), 113. doi: 10.3847/1538-4357/abed50

Mazelle, C., Winterhalter, D., Sauer, K., Trotignon, J., Acuña, M., Baumgärtel, K., … Slavin, J. (2004, March). Bow Shock and Upstream Phenomena at Mars. *Space Science Reviews*, *111*(1), 115–181. Retrieved 2019-10-14, from https://doi.org/10.1023/B:SPAC.0000032717.98679.d0 doi: 10.1023/B:SPAC.0000032717.98679.d0

McFadden, J. P., Kortmann, O., Curtis, D., Dalton, G., Johnson, G., Abiad, R., … Jakosky, B. (2015, December). MAVEN SupraThermal and Thermal Ion Compostion (STATIC) Instrument. *Space Sci Rev*, *195*(1), 199–256. Retrieved 2020-02-13, from https://doi.org/10.1007/s11214-015-0175-6 doi: 10.1007/s11214-015-0175-6

Merka, J., Szabo, A., Slavin, J. A., & Peredo, M. (2005). Three-dimensional position and shape of the bow shock and their variation with upstream Mach numbers and interplanetary magnetic field orientation. *Journal of Geophysical Research: Space Physics*, *110*(A4). Retrieved 2021-03-18, from http://agupubs.onlinelibrary.wiley.com/doi/abs/10.1029/2004JA010944 (_eprint: https://onlinelibrary.wiley.com/doi/pdf/10.1029/2004JA010944) doi: https://doi.org/10.1029/2004JA010944

Mitchell, D. L., Mazelle, C., Sauvaud, J.-A., Thocaven, J.-J., Rouzaud, J., Fedorov, A., … Jakosky, B. M. (2016, April). The MAVEN Solar Wind Electron Analyzer. *Space Sci Rev*, *200*(1), 495–528. Retrieved 2021-05-06, from https://doi.org/10.1007/s11214-015-0232-1 doi: 10.1007/s11214-015-0232-1

Möstl, C., Weiss, A., Bailey, R., Isavnin, A., Wedlund, C. S., Stansby, D., … Winslow, R. (2020). *Solar wind in situ data for creating catalogs and statistics of interplanetary coronal mass ejections and high speed streams (Solar Orbiter, Parker Solar Probe, STEREO-A/B, MAVEN, Wind, MESSENGER, VEX, Ulysses) 2007-2020.* Retrieved from https://figshare.com/articles/dataset/Coronal_mass_ejection_in_situ_data_for_creating_catalogs_and_statistics_MESSENGER_VEX_Wind_STEREO-A_B_MAVEN_PSP_2007-2019/11973693

Moullard, O., Burgess, D., Horbury, T. S., & Lucek, E. A. (2006). Ripples observed on the surface of the Earth's quasi-perpendicular bow shock. *Journal of Geophysical Research: Space Physics*, *111*(A9). Retrieved 2021-03-18, from http://agupubs.onlinelibrary.wiley.com/doi/abs/10.1029/2005JA011594 (_eprint: https://onlinelibrary.wiley.com/doi/pdf/10.1029/2005JA011594) doi: https://doi.org/10.1029/2005JA011594

Peredo, M., Slavin, J. A., Mazur, E., & Curtis, S. A. (1995). Three-dimensional position and shape of the bow shock and their variation with Alfvénic, sonic and magnetosonic Mach numbers and interplanetary magnetic field orientation. *Journal of Geophysical Research: Space Physics*, *100*(A5), 7907–7916. Retrieved 2021-03-18, from http://agupubs.onlinelibrary.wiley.com/doi/abs/10.1029/94JA02545

(_eprint: https://onlinelibrary.wiley.com/doi/pdf/10.1029/94JA02545) doi: https://doi.org/10.1029/94JA02545

Peredo, M., Stern, D. P., & Tsyganenko, N. A. (1993). Are existing magnetospheric models excessively stretched? *Journal of Geophysical Research: Space Physics*, *98*(A9), 15343–15354. Retrieved 2021-03-18, from http://agupubs.onlinelibrary.wiley.com/doi/abs/10.1029/93JA01150 (_eprint: https://onlinelibrary.wiley.com/doi/pdf/10.1029/93JA01150) doi: https://doi.org/10.1029/93JA01150

Ramstad, R., Barabash, S., Futaana, Y., & Holmström, M. (2017). Solar wind- and EUV-dependent models for the shapes of the Martian plasma boundaries based on Mars Express measurements. *Journal of Geophysical Research: Space Physics*, *122*(7), 7279–7290. Retrieved 2020-07-30, from http://agupubs.onlinelibrary.wiley.com/doi/abs/10.1002/2017JA024098 (_eprint: https://onlinelibrary.wiley.com/doi/pdf/10.1002/2017JA024098) doi: 10.1002/2017JA024098

Russell, C. T. (1977). On the relative locations of the bow shocks of the terrestrial planets. *Geophysical Research Letters*, *4*(10), 387–390. Retrieved 2020-02-04, from http://agupubs.onlinelibrary.wiley.com/doi/abs/10.1029/GL004i010p00387 doi: 10.1029/GL004i010p00387

Russell, C. T., Chou, E., Luhmann, J. G., Gazis, P., Brace, L. H., & Hoegy, W. R. (1988). Solar and interplanetary control of the location of the Venus bow shock. *J. Geophys. Res.*, *93*(A6), 5461. Retrieved 2019-09-20, from http://doi.wiley.com/10.1029/JA093iA06p05461 doi: 10.1029/JA093iA06p05461

Sánchez-Cano, B., Lester, M., Witasse, O., Milan, S. E., Hall, B. E. S., Cartacci, M., ... Pätzold, M. (2016). Solar cycle variations in the ionosphere of Mars as seen by multiple Mars Express data sets. *Journal of Geophysical Research: Space Physics*, *121*(3), 2547–2568. Retrieved 2021-03-18, from http://agupubs.onlinelibrary.wiley.com/doi/abs/10.1002/2015JA022281 (_eprint: https://onlinelibrary.wiley.com/doi/pdf/10.1002/2015JA022281) doi: https://doi.org/10.1002/2015JA022281

Schwartz, S. J. (1998). Shock and Discontinuity Normals, Mach Numbers, and Related Parameters. *ISSI Scientific Reports Series*, *1*, 249–270. Retrieved 2021-03-18, from http://adsabs.harvard.edu/abs/1998ISSIR...1..249S

Schwingenschuh, K., Riedler, W., Lichtenegger, H., Yeroshenko, Y., Sauer, K., Luhmann, J. G., ... Russell, C. T. (1990). Martian bow shock: Phobos observations. *Geophysical Research Letters*, *17*(6), 889–892. Retrieved 2020-08-03, from http://agupubs.onlinelibrary.wiley.com/doi/abs/10.1029/GL017i006p00889 (_eprint: https://onlinelibrary.wiley.com/doi/pdf/10.1029/GL017i006p00889) doi: 10.1029/GL017i006p00889

Simon Wedlund, C., Alho, M., Gronoff, G., Kallio, E., Gunell, H., Nilsson, H., ... Miloch, W. J. (2017, August). Hybrid modelling of cometary plasma environments: I. Impact of photoionisation, charge exchange, and electron ionisation on bow shock and cometopause at 67P/Churyumov-Gerasimenko. *A&A*, *604*, A73. Retrieved 2019-11-12, from http://www.aanda.org/10.1051/0004-6361/201730514 doi: 10.1051/0004-6361/201730514

Slavin, J. A., & Holzer, R. E. (1981, December). Solar wind flow about the terrestrial planets 1. Modeling bow shock position and shape. *Journal of Geophysical Research: Space Physics*, *86*(A13), 11401–11418. Retrieved 2019-10-15, from http://agupubs.onlinelibrary.wiley.com/doi/abs/10.1029/JA086iA13p11401 doi: 10.1029/JA086iA13p11401

Slavin, J. A., Holzer, R. E., Spreiter, J. R., & Stahara, S. S. (1984). Planetary Mach cones: Theory and observation. *Journal of Geophysical Research: Space Physics*, *89*(A5), 2708–2714. Retrieved 2020-08-03, from http://agupubs.onlinelibrary.wiley.com/doi/abs/10.1029/JA089iA05p02708 (_eprint: https://onlinelibrary.wiley.com/doi/pdf/10.1029/JA089iA05p02708) doi: 10.1029/JA089iA05p02708

Slavin, J. A., Schwingenschuh, K., Riedler, W., & Yeroshenko, Y. (1991). The solar wind interaction with Mars: Mariner 4, Mars 2, Mars 3, Mars 5, and Phobos 2 observations of bow shock position and shape. *Journal of Geophysical Research: Space Physics*, *96*(A7), 11235–11241. Retrieved 2020-02-04, from http://agupubs.onlinelibrary.wiley.com/doi/abs/10.1029/91JA00439 doi: 10.1029/91JA00439

Taubin, G. (1991, November). Estimation of Planar Curves, Surfaces, and Nonplanar Space Curves Defined by Implicit Equations with Applications to Edge and Range Image Segmentation. *IEEE Transactions on Pattern Analysis and Machine Intelligence*, *13*(11), 1115–1138. Retrieved 2021-03-04, from https://www.computer.org/

csdl/journal/tp/1991/11/i1115/13rRUNvgzaN (Publisher: IEEE Computer Society) doi: 10.1109/34.103273

Thiemann, E. M. B., Chamberlin, P. C., Eparvier, F. G., Templeman, B., Woods, T. N., Bougher, S. W., & Jakosky, B. M. (2017). The MAVEN EUVM model of solar spectral irradiance variability at Mars: Algorithms and results. *Journal of Geophysical Research: Space Physics*, *122*(3), 2748–2767. Retrieved 2021-03-18, from http://agupubs.onlinelibrary.wiley.com/doi/abs/10.1002/2016JA023512 (_eprint: https://onlinelibrary.wiley.com/doi/pdf/10.1002/2016JA023512) doi: https://doi.org/10.1002/2016JA023512

Trainer, M. G., Wong, M. H., McConnochie, T. H., Franz, H. B., Atreya, S. K., Conrad, P. G., ... Zorzano, M.-P. (2019). Seasonal Variations in Atmospheric Composition as Measured in Gale Crater, Mars. *Journal of Geophysical Research: Planets*, *124*(11), 3000–3024. Retrieved 2021-03-18, from http://agupubs.onlinelibrary.wiley.com/doi/abs/10.1029/2019JE006175 (_eprint: https://onlinelibrary.wiley.com/doi/pdf/10.1029/2019JE006175) doi: https://doi.org/10.1029/2019JE006175

Trotignon, J., Mazelle, C., Bertucci, C., & Acuña, M. (2006, April). Martian shock and magnetic pile-up boundary positions and shapes determined from the Phobos 2 and Mars Global Surveyor data sets. *Planetary and Space Science*, *54*(4), 357–369. Retrieved 2019-09-20, from https://linkinghub.elsevier.com/retrieve/pii/S0032063306000110 doi: 10.1016/j.pss.2006.01.003

Trotignon, J. G., Grard, R., & Klimov, S. (1991). Location of the Martian bow shock measurements by the plasma wave system on Phobos 2. *Geophysical Research Letters*, *18*(3), 365–368. Retrieved 2020-08-03, from http://agupubs.onlinelibrary.wiley.com/doi/abs/10.1029/91GL00025 (_eprint: https://onlinelibrary.wiley.com/doi/pdf/10.1029/91GL00025) doi: 10.1029/91GL00025

Trotignon, J. G., Grard, R., & Skalsky, A. (1993, March). Position and shape of the Martian bow shock: the Phobos 2 plasma wave system observations. *Planetary and Space Science*, *41*(3), 189–198. Retrieved 2019-10-10, from http://www.sciencedirect.com/science/article/pii/003206339390058A doi: 10.1016/0032-0633(93)90058-A

Verigin, M., Slavin, J., Szabo, A., Gombosi, T., Kotova, G., Plochova, O., ... Shugaev, F.

(2003). Planetary bow shocks: Gasdynamic analytic approach. *Journal of Geophysical Research: Space Physics*, *108*(A8). Retrieved 2020-08-06, from http://agupubs.onlinelibrary.wiley.com/doi/abs/10.1029/2002JA009711 (_eprint: https://onlinelibrary.wiley.com/doi/pdf/10.1029/2002JA009711) doi: 10.1029/2002JA009711

Vignes, D., Acuña, M. H., Connerney, J. E. P., Crider, D. H., Rème, H., & Mazelle, C. (2002, May). Factors controlling the location of the Bow Shock at Mars. *Geophysical Research Letters*, *29*(9), 42–1–42–4. Retrieved 2019-10-10, from http://agupubs.onlinelibrary.wiley.com/doi/10.1029/2001GL014513 doi: 10.1029/2001GL014513

Vignes, D., Mazelle, C., Rme, H., Acuña, M. H., Connerney, J. E. P., Lin, R. P., ... Ness, N. F. (2000, January). The solar wind interaction with Mars: Locations and shapes of the bow shock and the magnetic pile-up boundary from the observations of the MAG/ER Experiment onboard Mars Global Surveyor. *Geophysical Research Letters*, *27*(1), 49–52. Retrieved 2019-10-10, from http://agupubs.onlinelibrary.wiley.com/doi/10.1029/1999GL010703 doi: 10.1029/1999GL010703

Volwerk, M., Schmid, D., Tsurutani, B. T., Delva, M., Plaschke, F., Narita, Y., ... Glassmeier, K.-H. (2016, November). Mirror mode waves in Venus's magnetosheath: solar minimum vs. solar maximum. *Ann. Geophys.*, *34*(11), 1099–1108. Retrieved 2019-09-10, from https://www.ann-geophys.net/34/1099/2016/ doi: 10.5194/angeo-34-1099-2016

Yamauchi, M., Hara, T., Lundin, R., Dubinin, E., Fedorov, A., Sauvaud, J. A., ... Barabash, S. (2015, December). Seasonal variation of Martian pick-up ions: Evidence of breathing exosphere. *Planetary and Space Science*, *119*, 54–61. Retrieved 2021-03-18, from https://www.sciencedirect.com/science/article/pii/S0032063315002639 doi: 10.1016/j.pss.2015.09.013

Zhang, T., Delva, M., Baumjohann, W., Volwerk, M., Russell, C., Barabash, S., ... Zambelli, W. (2008, May). Initial Venus Express magnetic field observations of the Venus bow shock location at solar minimum. *Planetary and Space Science*, *56*(6), 785–789. Retrieved 2019-09-20, from https://linkinghub.elsevier.com/retrieve/pii/S0032063307003777 doi: 10.1016/j.pss.2007.09.012

Zhang, T. L., Schwingenschuh, K., Lichtenegger, H., Riedler, W., Russell, C. T., & Luh-

mann, J. G. (1991). Interplanetary magnetic field control of the Mars bow shock: Evidence for Venuslike interaction. *Journal of Geophysical Research: Space Physics*, *96*(A7), 11265–11269. Retrieved 2020-08-03, from http://agupubs.onlinelibrary.wiley.com/doi/abs/10.1029/91JA01099 (_eprint: https://onlinelibrary.wiley.com/doi/pdf/10.1029/91JA01099) doi: 10.1029/91JA01099

Zhang, T.-L., Schwingenschuh, K., Russell, C. T., & Luhmann, J. G. (1991). Asymmetries in the location of the Venus and Mars bow shock. *Geophysical Research Letters*, *18*(2), 127–129. Retrieved 2019-11-29, from http://agupubs.onlinelibrary.wiley.com/doi/abs/10.1029/90GL02723 doi: 10.1029/90GL02723

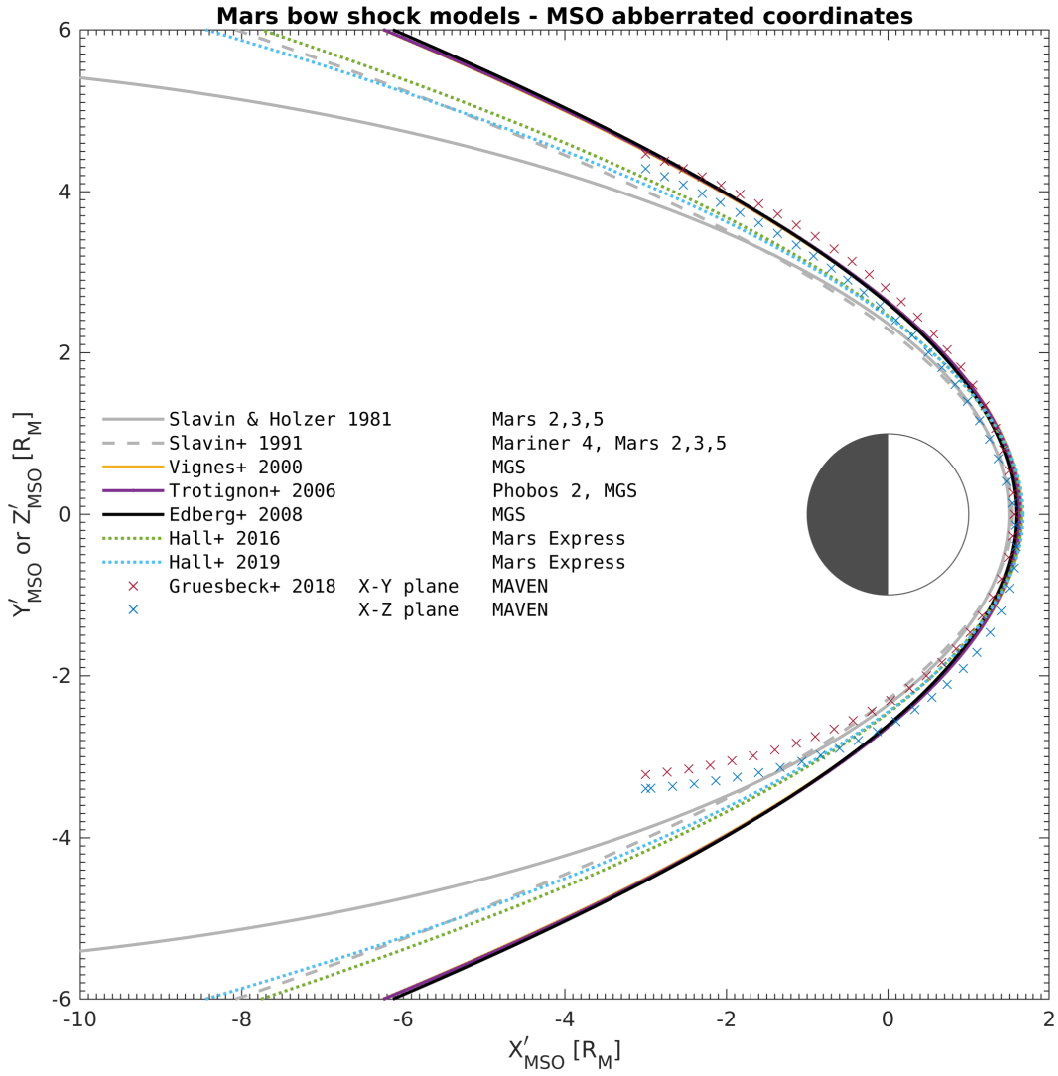

Figure 3. Bow shock fitted models to observations in MSO aberrated coordinates. The 3D quadratic model of Gruesbeck et al. (2018) fitted from MAVEN data was rotated anticlockwise 4° around the Z axis. All other models are obtained in cylindrical conic form from other missions, including Mars Express (MEX), Mars Global Surveyor (MGS), Phobos 2 and the Mars 2-3-5 missions. The fits of Hall et al. (2016), Hall et al. (2019) and Gruesbeck et al. (2018) consider all shock detection points of their respective studies. Because the cylindrical models are symmetric about the X' axis, the figure's cylindrical y-axis $\sqrt{Y'^2 + Z'^2}$ is equivalent to the Y' or to the Z' axis, regardless.

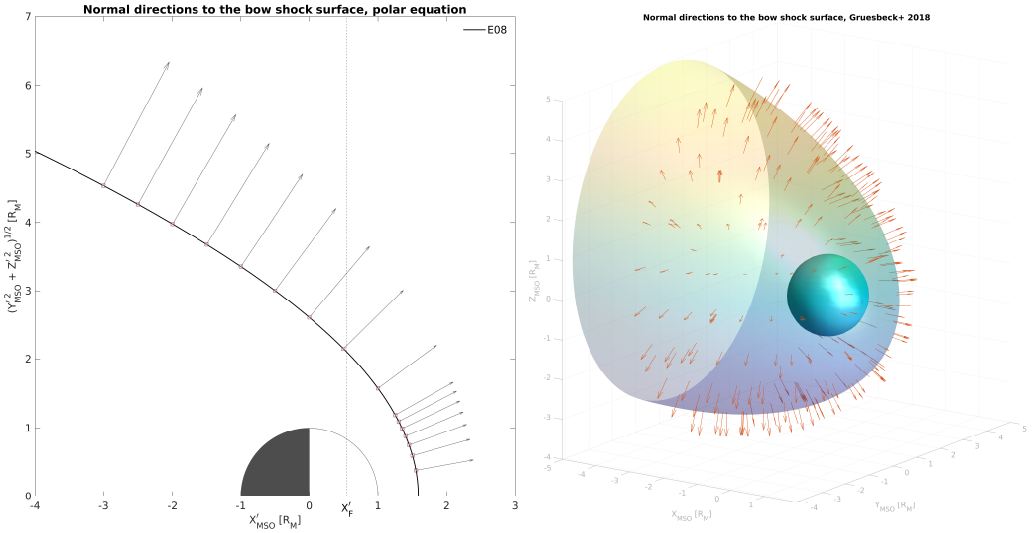

Figure 4. Bow shock normal in the polar 2D case (left, model of Edberg et al., 2008) and in the Cartesian 3D case (right, model of Gruesbeck et al., 2018).

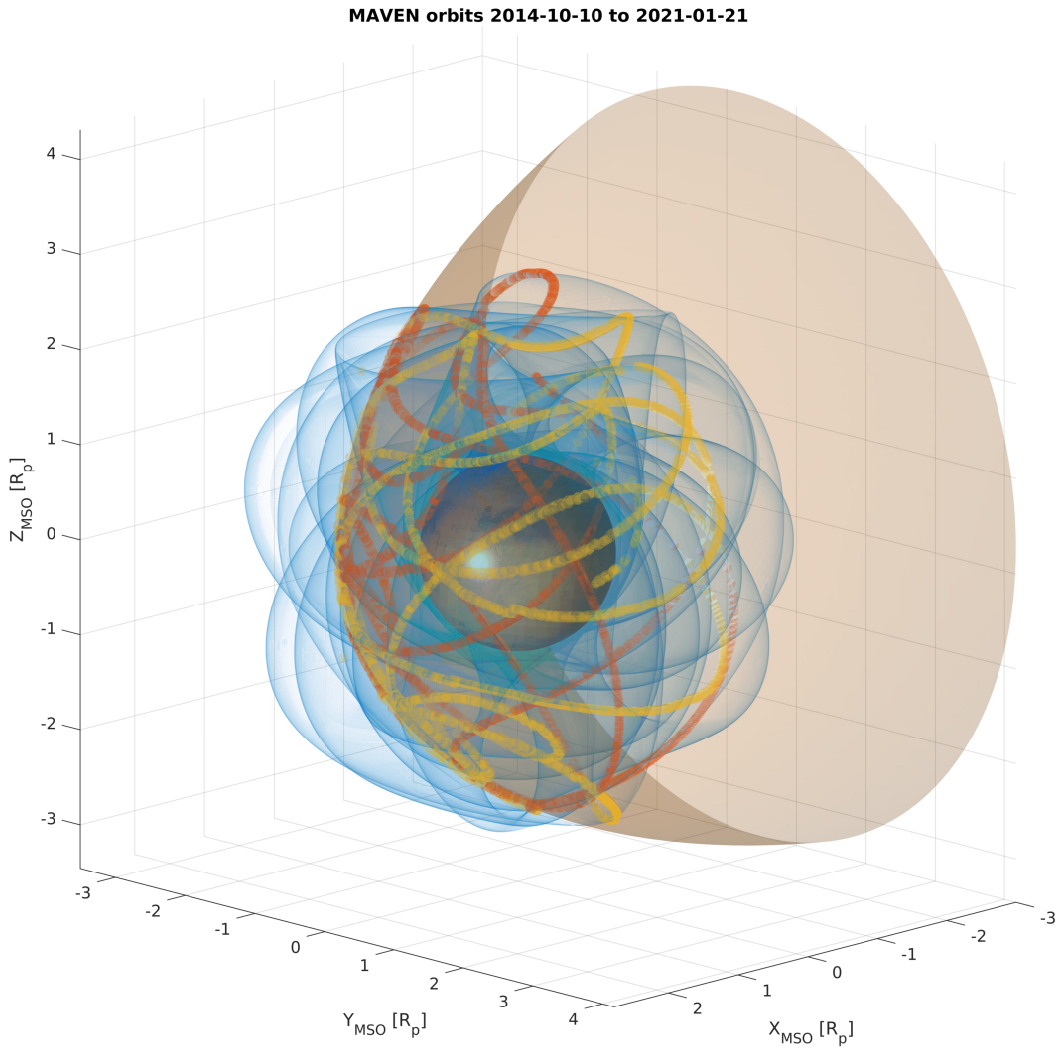

Figure 5. Automatic detection of bow shock in MSO coordinates normalised to the planet's radius, using the general quadric formula of Gruesbeck et al. (2018). The bow shock surface is in brown, the orbit of MAVEN between 01 November 2014 and 07 February 2021 is in blue. Detections of the crossings from inside the shock surface to outside of it are shown as orange circles, whereas outside-to-inside crossings are depicted by yellow circles.

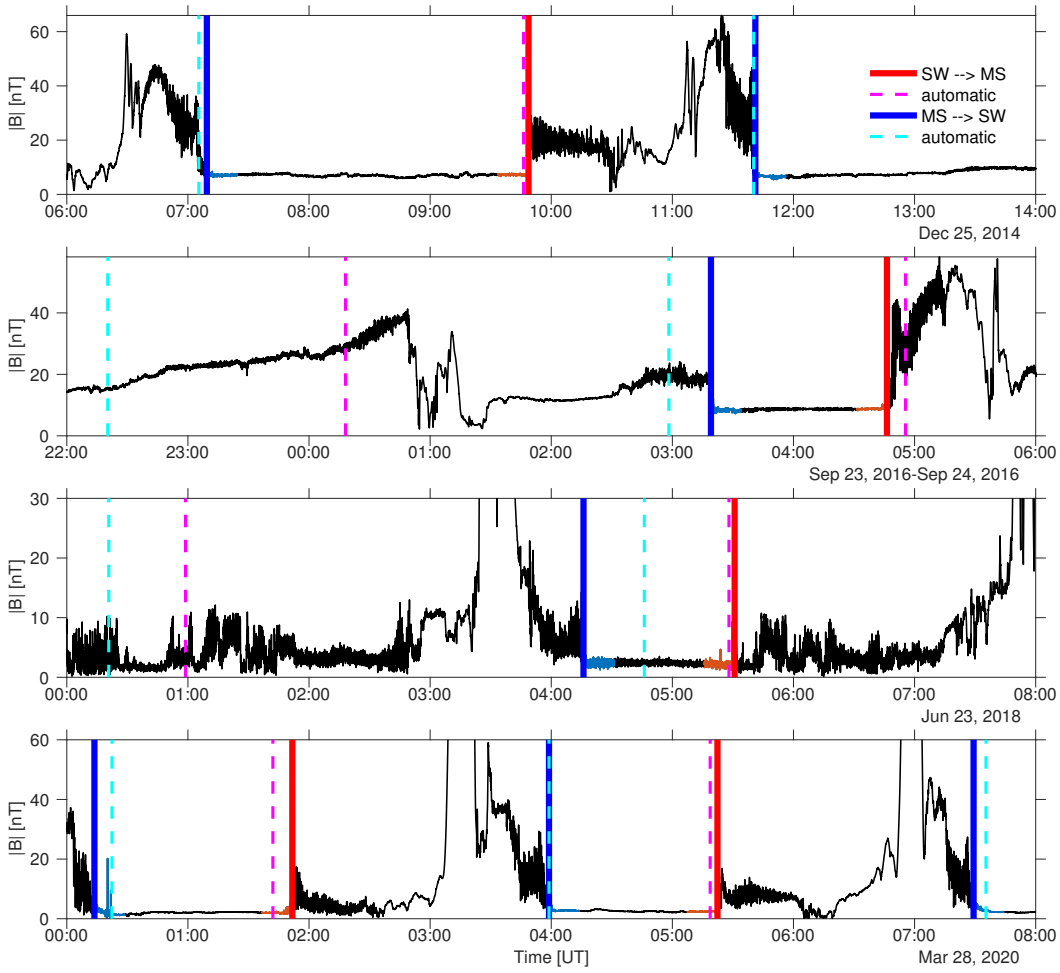

Figure 6. Examples of total magnetic field amplitudes at 1 s resolution measured by the MAVEN/MAG instrument throughout the mission. Top panel: 25 Dec. 2014 (beginning of mission). The first crossing is quite oblique ($\theta_{Bn} \approx 45°$) followed by two highly $q_\perp$ shock crossings ($\theta_{Bn} > 85°$). Second panel: 23-24 Sept. 2016. The two selected crossings are $q_\perp$, the first one with $\theta_{Bn} \approx 58°$, the second with $\theta_{Bn} \approx 78°$. Third panel: 23 June 2018, with two $q_\parallel$ crossings ($\theta_{Bn} \approx 8, 25°$). Bottom panel: 28 March 2020, with five crossings all oblique towards $q_\perp$ conditions, with $\theta_{Bn} \approx 45°, 49°, 80°, 82°$ and $88°$, successively. The predictor geometric detections (Sect. 3.1) are in dashed lines and labelled "automatic", whereas the predictor-corrector detections proposed in Sect. 3.2 are in solid lines. Highlighted in different colours are crossings from solar wind to magnetosheath (labelled $SW \rightarrow MS$, red) and from magnetosheath to solar wind (labelled $MS \rightarrow SW$, blue). Calculations of θ_{Bn} angles were performed using median averages of **B** over the colour-highlighted regions (blue for $MS \rightarrow SW$ crossings, red for $SW \rightarrow MS$ crossings).

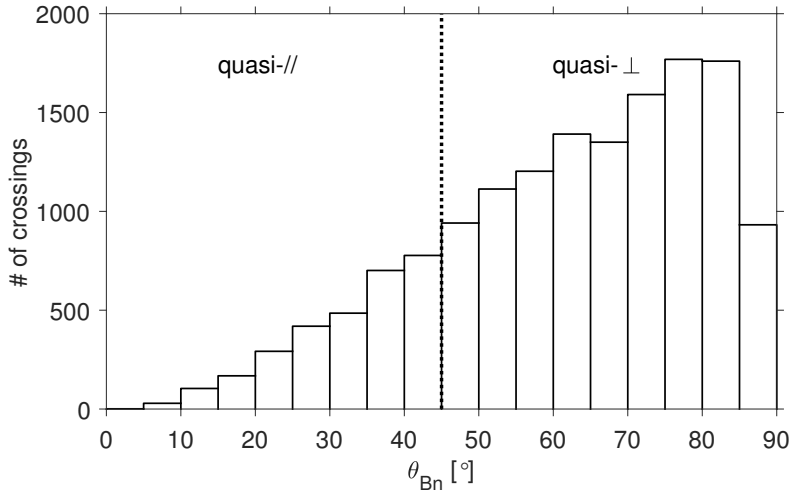

Figure 7. Statistical distribution of crossings with respect to θ_{Bn} angles, the angle between the normal to the shock and the average magnetic field direction. The limit between $q_{\|}$l and $q_{\perp}$ conditions is for $\theta_{Bn} = 45°$.

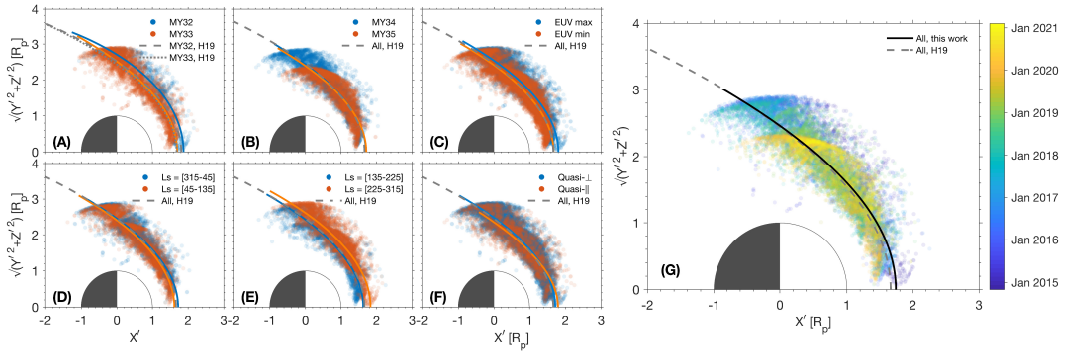

Figure 8. 2D fits performed on the predictor-corrector algorithm for the detection of bow shock crossings in the MAVEN dataset, 2014 – 2021 in aberrated MSO coordinates ($X'_{\mathrm{MSO}}, Y'_{\mathrm{MSO}}, Z'_{\mathrm{MSO}}$), and parametrised in Table 3. Panels (A) and (B): vs Martian Years 32 to 35. Panels (C) and (D): vs Ls (season) ranges. Panel (E): vs EUV flux levels. Panel (F): vs shock nature ($q_{\perp}$ and $q_{\|}$). Panel (G): all detected points in the current database colour-coded by year, and comparison to the analytical quadric fit of Hall et al. (2019). All coordinates are expressed in units of the planet's radius, i.e., R_{p} = 3389.5 km. Superimposed on all panels are the corresponding analytical models of Hall et al. (2019) for Martian years 27–33, except for Martian years 32 and 33, where their corresponding yearly fits are plotted. Candidate detections points for each case are also drawn as filled circles of varying colours, with the opacity giving a measure of the density of points in that area, giving more or less weight to the fitting method.

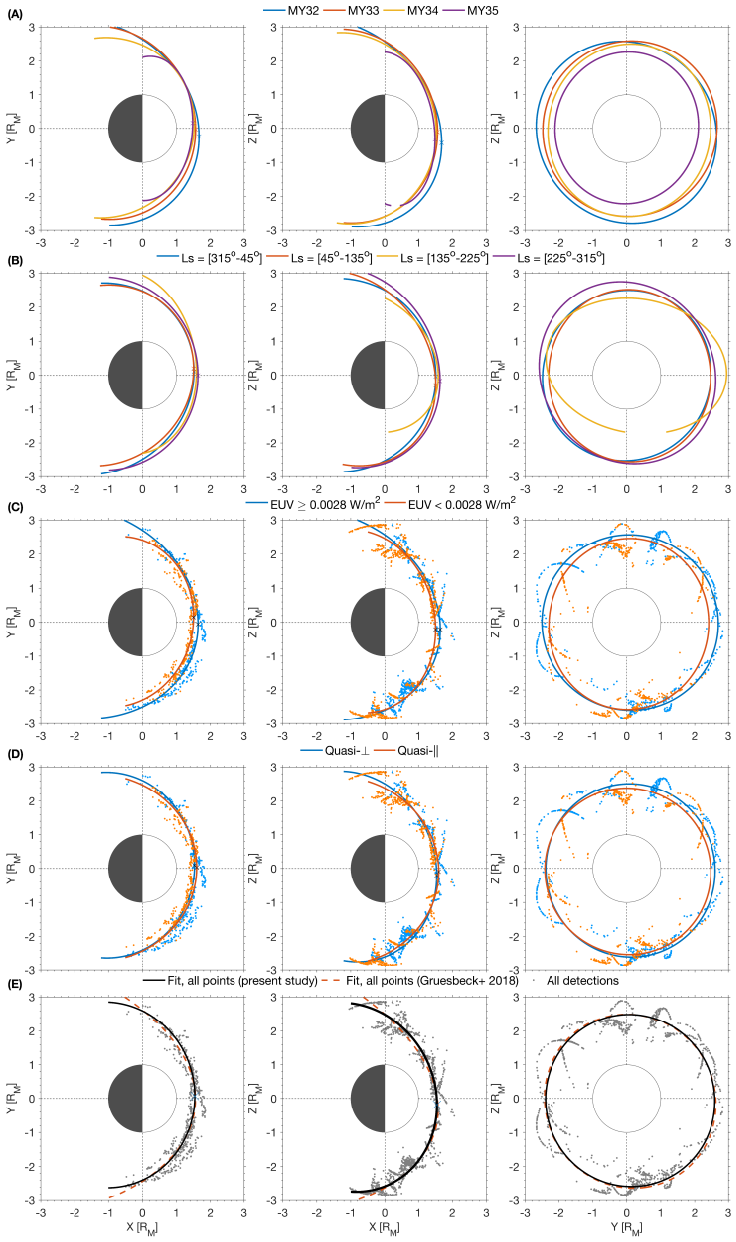

Figure 9. 3D fits performed on the refined predictor-corrector algorithm for the detection of bow shock crossings in the MAVEN dataset, 2014 – 2021 in the $X_{\mathrm{MSO}} - Y_{\mathrm{MSO}}$, $X_{\mathrm{MSO}} - Y_{\mathrm{MSO}}$ and $Y_{\mathrm{MSO}} - Z_{\mathrm{MSO}}$ planes (traces of ellipsoids of revolution parametrised in Table 4). (A) vs Martian Years. (B) vs Ls (season) ranges. (C) vs EUV flux levels, with their corresponding subset of detected points (blue and orange dots). (D) vs bow shock nature, $q_{\perp}$ (blue dots) and $q_{\parallel}$ (orange dots). (E) all detected points in the current database with a comparison of present fit (black line) to the analytical quadric fit of Gruesbeck et al. (2018) (orange dashed line). On each figure, superimposed crosses show where the nose of the shock is located, in the plane of projection (see Appendix Appendix B). All coordinates are expressed in units of the planet's radius, i.e., $R_{\mathrm{p}} = 3389.5$ km.

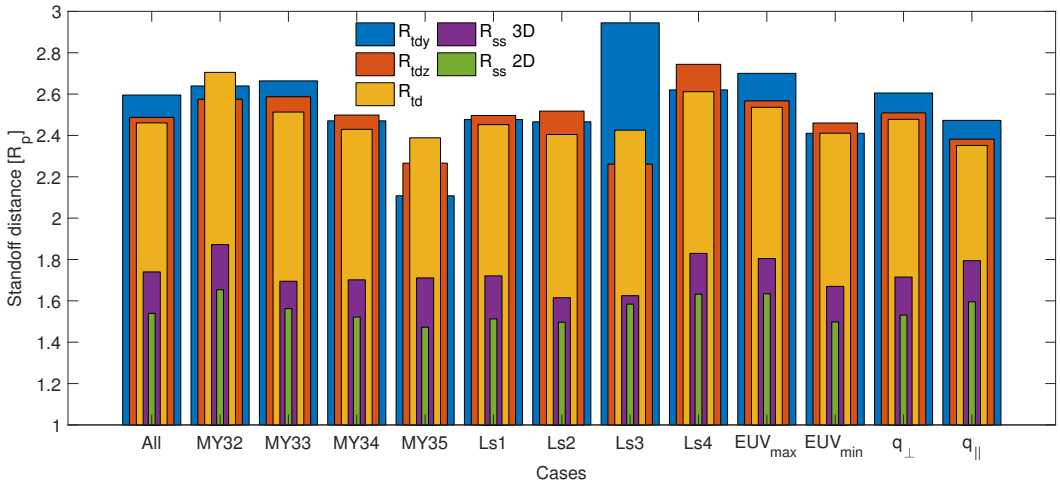

Figure 10. Comparison of standoff distances, both at the subsolar point and at the terminator, calculated from the 2D and 3D fits, and for each case as in Tables 3 and 4. Terminator standoff values are in blue, orange and yellow (wider bars), whereas subsolar standoff values are in violet and green (thinner bars). For brevity in the axis labelling, Ls1 = [315° − 45°], Ls2 = [45° − 135°], Ls3 = [135° − 225°], Ls4 = [225° − 315°]. All distances are expressed in units of the planet's radius, i.e., $R_\mathrm{p} = 3389.5$ km.